Direct measurement of orientation correlations in a two-dimensional liquid-crystal system

David H. Van Winkle
Department of Physics, Florida State University, Tallahassee, Florida 32306-3016

Noel A. Clark
Department of Physics, University of Colorado, Boulder, Colorado 80309-0390
(Received 24 August 1987; revised manuscript received 11 April 1988)

The behavior of a two-dimensional orientation field has been studied directly in space and time. In a freely suspended thin film of tilted smectic liquid crystal the local projection onto the film plane of the molecular orientation averaged through the film forms a two-dimensional (2D) vector field $\hat{\mathbf{C}}(x,y)$ with local orientation $\Phi(x,y)$. This orientation field was imaged in real space by depolarized reflection microscopy. By probing the light at two distinct (x,y) locations in the image and employing cross-correlation intensity-fluctuation spectroscopy, we have measured the space-time behavior of $\sigma^2(\boldsymbol{\rho},\tau)\equiv\langle\,|\Phi(\mathbf{0},0)-\Phi(\boldsymbol{\rho},\tau)|^2\rangle$. At large τ, σ increases logarithmically with τ, consistent with the expected diffusional dynamics and thermally excited fluctuation spectrum of Φ. This logarithmic (Landau-Peierls) divergence confirms that this 2D orientational system is at its lower marginal dimensionality. In addition, by fitting the behavior of $\sigma^2(\boldsymbol{\rho},\tau)$, we extract the 2D orientational diffusion constants for splay and bend in both the smectic-C and smectic-I phases.

I. INTRODUCTION

A. Freely suspended liquid-crystal films (FSLCF's)

In 1922 Friedel reported that stable smectic liquid-crystal films could be suspended in air across a hole.[1] During the early 1970s Clark and Meyer showed that such freely suspended smectic films as thin as two molecular layers could be formed and remain stable for many months. They suggested and demonstrated that these very thin films could be useful systems for the study of surface interactions and the effects of reduced dimensionality on liquid-crystal phase transitions.[2] The richness of bulk liquid-crystal phase diagrams is enhanced in FSLCF's by the additional variable of film thickness, which suggests the possibility of observing three- to two-dimensional (3D-2D) crossover in the phase diagram in thin enough films.[3] Also, it has been proposed that in a 2D system the crystal-liquid phase transition includes an intermediate bond orientationally ordered "hexatic" phase.[4] Evidence consistent with the existence of a hexatic phase has been obtained in x-ray scattering studies of FSLCF's.[5] Recently a number of elegant experiments probing the observable consequences of bond-orientational order in the smectic-I phase have appeared.[6] Another interesting fundamental property of 2D systems is that certain kinds of order will diverge logarithmically with system size; one example is positional order in a crystal. This is the so-called Landau-Peierls divergence of order in a system at its lower critical dimension. For a FSLCF in a tilted phase, the projection of the molecular long axis in the plane of the film forms a 2D orientation field which should exhibit this logarithmic divergence in order. We report here an investigation of such a system at its lower critical dimension using a new experimental technique to directly observe the Landau-Peierls divergence in space and time.

To study the 2D orientation field we constructed a polarized reflection microscope using an argon-ion laser as the illuminator, forming a real in-plane image of the tilted smectic FSLCF. In this image, light intensity is determined by molecular orientation. Thus, information about the behavior of molecular-orientational order (not bond-orientational order) may be obtained by observing the spatial and temporal characteristics of the depolarized reflected light. Light from two spatially separated regions in the image is transmitted to photon detecting and counting electronics by fiber optics. The intensity-intensity time cross-correlation function is obtained by sequential summation of the product of the intensity at the first probe and the intensity at the second probe at delayed times. The mean-square orientation difference between the two regions is then calculated from the correlation function.

Our results verify the dimensionality of the 2D orientation field and accentuate some consequences of the low dimensionality. The Landau-Peierls divergence in order is observed as a logarithmic increase with time of the mean-square orientation difference at the two probes at extremely long time delays and large spatial separations. We also observed contributions to the cross-correlation function which would probably not be noticed in an autocorrelation experiment, either in real space or in the reciprocal space of a scattering experiment. There is a nonlinear dependence of the reflected intensity on director orientation. The amplitude of orientation fluctuations in this 2D system is so large that a scattering or imaging geometry for which the intensity fluctuates only linearly with the orientation cannot be found. Two modes of elastic relaxation exist for orientation fluctuations, and the particular modes available are energetically quite anisotropic.[7,8] Cross-correlation functions obtained for these

separate modes appear to be qualitatively different, though we propose an explanation involving fourth-order coupling of orientation fluctuations to the reflected intensity which satisfactorily explains the data.

B. Tilted phase FSLCF's

For a FSLCF in a tilted smectic phase there will be a projection of the molecular director $\hat{\mathbf{n}}(\mathbf{r})$ in the film (x,y) plane, which defines the unit vector C director, $\tilde{C}(x,y,z)$. The orientation of $\tilde{C}(x,y,z)$ is specified by the angle $\tilde{\Phi}(x,y,z)$, the azimuthal orientation of $\hat{\mathbf{n}}(\mathbf{r})$. Our experiment probes $\Phi(x,y)$, the z average of $\tilde{\Phi}(x,y,z)$:

$$\Phi(x,y)\equiv\int_{-L/2}^{L/2} dz\,\tilde{\Phi}(x,y,z)\ , \tag{1}$$

where L is the thickness of the film and the origin of the coordinate system is chosen to be the film center. Figure 1 shows this geometry for a three-layer film. The order parameter for a smectic-C phase incorporates both the tilt angle θ_T and the azimuthal orientation, as $\Psi=\theta_T\exp(i\tilde{\Phi})$. Thermal fluctuations in Ψ contribute to the free energy via a term in $|\Psi|^2$ associated with tilt-angle fluctuations and terms in $(\nabla\Psi)^2$ associated with azimuthal orientation fluctuations. The free energy of the $|\Psi|^2$ term is

$$F=\tfrac{1}{2}B(\theta_T-\langle\theta_T\rangle)^2\ . \tag{2}$$

Except very near the smectic-A-to-smectic-C (SmA-SmC) transition at which $\theta_T\to 0$ continuously in a second-order phase transition, the elastic constant B is of order k_BT/(molecule rad^2). Since our experiment is optical, the minimum area probed is $\approx 1\ \mu$m^2 and contains $\approx 10^6$ molecules. Hence, fluctuations in θ_T averaged over the minimum probed area are of order $(10^{-6})^{1/2}$ rad and can be ignored. By contrast, fluctuations in the azimuthal angle $\tilde{\Phi}$ are suppressed only by $\nabla\Psi$ and are significant.

We examine the dynamics of $\Phi(x,y)$ and explain fluctuations in Φ using a 2D model of orientational order. To the extent that the experiment conceived probes only the z average orientation $\Phi(x,y)$, the FSLCF models a 2D system and $\hat{\mathbf{C}}(x,y)$ approximates a 2D nematic director field. The free energy of a 2D nematic in the absence of external fields is

$$F-F_0=[\tfrac{1}{2}K_B(\nabla\times\hat{\mathbf{C}})^2+\tfrac{1}{2}K_S(\nabla\cdot\hat{\mathbf{C}})^2]\ , \tag{3}$$

where the bend orientational elastic constant K_B is associated with the curl of the orientation field defined by $\hat{\mathbf{C}}$, and the splay elastic constant K_S is associated with the divergence of $\hat{\mathbf{C}}$. A characteristic of a nematic is that $\hat{\mathbf{n}}(\mathbf{r})$ is equivalent to $-\hat{\mathbf{n}}(\mathbf{r})$, whereas in the tilted smectic FSLCF $\hat{\mathbf{C}}(x,y)$ is not equivalent to $-\hat{\mathbf{C}}(x,y)$. The significant consequence of this distinction is a restriction on strength of allowed disclinations in the orientation field.

Most of the measurements reported here were on a racemic mixture of DOBAMBC,[9] a chiral molecule. In a five-layer liquid-crystal film, DOBAMBC has the following phase diagram:

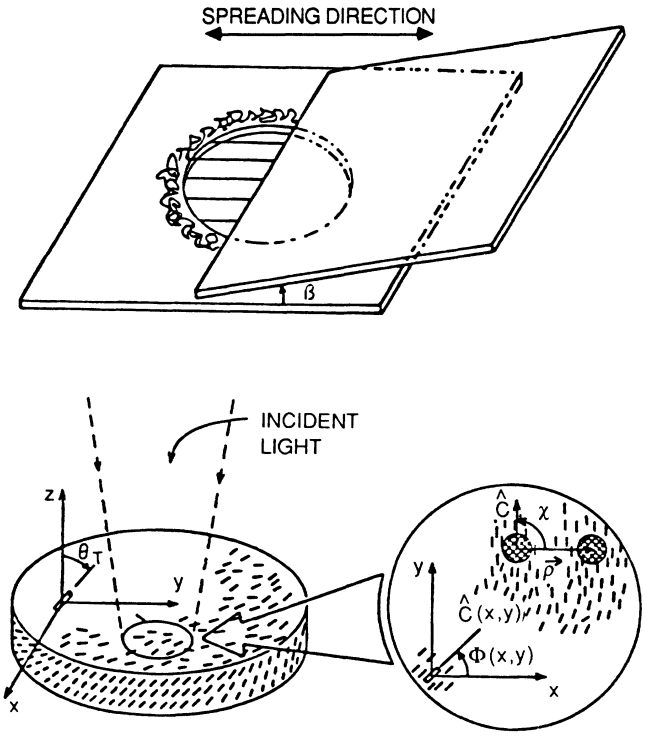

FIG. 1. A FSLCF is formed by placing a smectic liquid crystal between a substrate and spreader then drawing the hole in the substrate past the spreader. The geometry of the tilted smectic film is shown. The molecules are tilted an angle θ_T from perpendicular to the film. The projection of the director $\hat{\mathbf{n}}(\mathbf{r})$ in the film plane is $\hat{\mathbf{C}}(x,y)$ and has azimuthal orientation $\Phi(x,y)$. The cross-hatched regions represent fiber-optic probes in the image separated by ρ. The angle between $\hat{\mathbf{C}}(x,y)$ and ρ defines χ.

$$\text{Crystal}\xrightarrow{76^\circ\text{C}}\text{Sm}C\xleftrightarrow{120^\circ\text{C}}\text{Sm}A\leftrightarrow\text{Isotropic}\ .$$
$$\text{Sm}I\ \ (65^\circ\text{C})$$

DOBAMBC was the first liquid crystal discovered to be ferroelectric and was synthesized at Université de Paris–Sud (France) in the early 1970s.[10] It is fundamentally interesting as a ferroelectric liquid crystal, but in our experiment the racemic mixture gives zero net polarization, hence it is not ferroelectric. We use DOBAMBC because independent measurements of the orientational elastic properties of FSLCF's of DOBAMBC are available.[7]

C. *XY* model

The 2D XY model was initially developed to describe a 2D ferromagnet with degenerate energy upon a uniform rotation of the spins.[11] The Hamiltonian for the 2D XY model is

$$H=\int d^2\rho\,J[\nabla^2\Phi(\rho)]\ , \tag{4}$$

where J is a coupling constant, Φ labels the orientation of the spins, and ρ is the space variable. This model has

proved applicable to 2D superfluid ^{4}He,[12] superconductor,[13] and Coulomb gas[14] systems. The FSLCF is slightly more complex since the coupling constants K_S and K_B are different. However, if $K=K_S=K_B$ and q is the momentum space wave vector in the (x,y) plane, the characteristic energy for the FSLCF, L^2qK, reduces to the energy L^2qJ characteristic of the XY model. The long-wavelength fluctuations in molecular orientation we study are the so-called spin waves of the XY model.

D. Landau-Peierls divergence

One aspect of a system displaying order in one or two dimensions is the Landau-Peierls (LP) divergence of that order with system size. Landau and Peierls independently showed that infinite one- or two-dimensional systems could exhibit long-range order only at zero temperature. If Φ defines a fluctuating variable, then as $q\rightarrow 0$ the mean-square fluctuation in Φ, $\langle \Phi_q \Phi_{-q} \rangle$, does not diverge in 3D, diverges as $\ln(q)$ in 2D, and as $1/q$ in one dimension.[15] In 2D a quasi-long-range-order (QLRO) regime can be defined, bounded by a correlation length ξ. For lengths greater than ξ, fluctuations are larger than the characteristic periodicity of Φ, destroying long-range order. In the XY model, $\xi = a\exp(\pi J/k_B T)$, where a is a small-length characteristic of the system.[11]

II. ORIENTATION FLUCTUATIONS IN TILTED SMECTIC FSLCF'S

A. Two dimensionality

FSLCF's are 3D systems. We now discuss the conditions under which they behave as 2D systems. Examine the 3D orientation field described by $\hat{\mathbf{n}}(\mathbf{r})$ in the limit of a thin tilted smectic slab with free surfaces and layers parallel to the (X,Y) plane. The short axis of the slab is along the z axis. The director fluctuates azimuthally about z with orientation $\tilde{\Phi}(\mathbf{r},z)$, where $\mathbf{r}=(x,y)$ are planar coordinates in the slab. There will exist fluctuations in $\tilde{\Phi}$ with wave vectors having a continuous distribution of x and y components [between a molecular size (a) cutoff $2\pi/a$ and a system size (R) cutoff $2\pi/R$]. Wave vectors along the z axis are quantized and have free surface boundary conditions. The zero surface torque implies z behavior of the form $\sin[(2l+1)\pi z/L]$ and $\cos(2l\pi z/L)$, where L is the thickness of the slab, the origin is chosen in the center of the slab, and l is an integer reflecting quantization of modes of fluctuation available perpendicular to the film plane. The orientation field as a function of position in the slab is

$$\tilde{\Phi}(\mathbf{r},z)=\sum_{l=0}^{\infty}\int_{2\pi/R}^{2\pi/a}\frac{d^2q}{4\pi^2}e^{i\mathbf{q}\cdot\mathbf{r}}[\Phi_s(\mathbf{q},l)\sin q_l z + \Phi_c(\mathbf{q},l)\cos q_l z]\ , \quad (5)$$

where $\mathbf{q}$ is the wave-vector component in the (X,Y) plane and q_l is the discrete wave-vector component along z, and the usual inverse relations hold, e.g.,

$$\Phi_s(\mathbf{q},l)=\frac{2}{AL}\int_{-L/2}^{L/2}dz\int_A d^2r\,\tilde{\Phi}(\mathbf{r},z)e^{-i\mathbf{q}\cdot\mathbf{r}}\sin(q_l z)\ , \quad (6)$$

with A the slab area. The $\Phi_c(\mathbf{q},l)$ are defined similarly. We make the one constant approximation $\tilde{K}=\tilde{K}_1=\tilde{K}_2=\tilde{K}_3$, which is not strictly correct, but the error will not affect this discussion. The free energy associated with orientation fluctuations in the slab for the one constant approximation $F=\int d^2r\,\tilde{K}/2(\nabla\tilde{\Phi})^2$ becomes under Fourier transformation

$$F=\frac{\tilde{K}}{4}\sum_l\sum_q[\,|\Phi_s(\mathbf{q},l)|^2+|\Phi_c(\mathbf{q},l)|^2](q^2+q_l^2)\ , \quad (7)$$

and from equipartition the thermal average of mean-square fluctuations $\langle|\Phi(\mathbf{q},l)|^2\rangle = 2k_BT/\tilde{K}(q^2+q_l^2)$. Now we calculate for two distinct points in the slab separated by $\boldsymbol{\rho}=\mathbf{r}_1-\mathbf{r}_2$ the mean-square orientation difference $\sigma^2(\boldsymbol{\rho},z_1,z_2)$:

$$\begin{aligned}\sigma^2(\boldsymbol{\rho},z_1,z_2)&\equiv\langle|\tilde{\Phi}(0,z_1)-\tilde{\Phi}(\boldsymbol{\rho},z_2)|^2\rangle\\&=\frac{A}{4\pi^2}\int d^2q\sum_l\{\langle|\Phi_s(\mathbf{q},l)|^2\rangle[\sin^2(q_lz_1)+\sin^2(q_lz_2)-2e^{i\mathbf{q}\cdot\boldsymbol{\rho}}\sin(q_lz_1)\sin(q_lz_2)]\\&\quad+\langle|\Phi_c(\mathbf{q},l)|^2\rangle[\cos^2(q_lz_1)+\cos^2(q_lz_2)-2e^{i\mathbf{q}\cdot\boldsymbol{\rho}}\cos(q_lz_1)\cos(q_lz_2)]\}\ . \quad (8)\end{aligned}$$

In our experiments the average orientation of $\tilde{\Phi}(\boldsymbol{\rho},z)$ along the z axis is probed [cf. Eq. (1)]. For this case the integrations over z involving $\sin^2(q_lz_i)$ and $\cos^2(q_lz_i)$ $(i=1,2)$ yield constants. All terms now are proportional to $[1-\exp(i\mathbf{q}\cdot\boldsymbol{\rho})]\langle|\Phi|^2\rangle$ and the resulting mean-square orientation difference is

$$\begin{aligned}\sigma^2(\boldsymbol{\rho})&=\langle|\Phi(0)-\Phi(\boldsymbol{\rho})|^2\rangle\\&=\frac{2k_BT}{\tilde{K}L}\int\frac{d^2q}{4\pi^2q^2}(1-e^{i\mathbf{q}\cdot\boldsymbol{\rho}})\ . \quad (9)\end{aligned}$$

This is exactly $\sigma^2(\boldsymbol{\rho})$ for separate points in a strictly 2D nematic-orientation field. This equivalence is the basis of the claim that the reported experiments probe a 2D system. Equation (9) was first obtained for a 2D nematic phase by de Gennes, whose calculation is not readily available in the literature and which we therefore now review.

B. de Gennes's model

de Gennes described the static and dynamic orientational order of a hypothetical 2D nematic phase of long

molecules on a fluid surface.[16] The free energy of the 2D nematic phase, given in Eq. (3), accounts for the spin-wave distortions in $\hat{\mathbf{C}}(x,y)$, in the absence of disclinations. de Gennes used the one constant approximation, where $K=K_S=K_B$ and Eq. (3) reduces to exactly the Hamiltonian for the XY model, given in Eq. (4) with the 2D Frank constant K replacing $2J$. Using this model de Gennes calculated

$$\sigma^2(\boldsymbol{\rho},\tau)\equiv\langle\,|\,\Phi(\mathbf{0},0)-\Phi(\boldsymbol{\rho},\tau)\,|^2\rangle\ ,$$

the mean-square orientation difference for a pair of distinct space-time points where the origin is redefined at one of the points. The time-dependent orientation $\Phi(\boldsymbol{\rho},\tau)$ may be written as a sum over independent modes in reciprocal space as follows:

$$\Phi(\boldsymbol{\rho},\tau)=\frac{L^2}{4\pi^2}\int d^2q\,e^{i\mathbf{q}\cdot\boldsymbol{\rho}}\Phi_q(\tau)$$

$$=\sum_q\Phi_q(\tau)e^{i\mathbf{q}\cdot\boldsymbol{\rho}}\ . \tag{10}$$

Writing the free energy in terms of these Fourier coefficients gives

$$F-F_0=\int d^2\rho\frac{K}{2}\sum_q\left[\left|\frac{\partial}{\partial x}[\Phi_q(\tau)e^{i\mathbf{q}\cdot\boldsymbol{\rho}}]\right|^2+\left|\frac{\partial}{\partial y}[\Phi_q(\tau)e^{i\mathbf{q}\cdot\boldsymbol{\rho}}]\right|^2\right]\ . \tag{11}$$

Doing the spatial derivatives introduces a factor of q and the thermal average free energy is

$$\langle F-F_0\rangle=(K/2)\sum_q q^2\langle\,|\,\Phi_q(\tau)\,|^2\rangle\ ,$$

with $\langle\,|\,\Phi_q\,|^2\rangle=k_BT/Kq^2$ for all q. We have implicitly assumed $\Phi(\boldsymbol{\rho},\tau)$ is a Gaussian random variable, therefore $\langle\,|\,\Phi(\mathbf{0},0)\,|^2\rangle=\langle\,|\,\Phi(\boldsymbol{\rho},\tau)\,|^2\rangle$ so that

$$\sigma^2(\boldsymbol{\rho},\tau)=2\langle[\,|\,\Phi(\mathbf{0},0)\,|^2-|\,\Phi(\mathbf{0},0)\Phi(\boldsymbol{\rho},\tau)\,|\,]\rangle\ . \tag{12}$$

The dynamic behavior of a nematic-orientation field involves both coupling of fluid flow to orientation and torques derived from thermal distortions of the elastic free energy as described by Eq. (3). As in three dimensions the viscous relaxations are orders of magnitude faster than orientation relaxations and effectively decouple,[17] leaving a single orientational diffusion process characterized by a diffusion constant $D=K/\eta$, where η is the isotropic orientational viscosity in the one constant approximation. The time correlation function of a mode of wave vector q has the form

$$\langle\Phi_q(0)\Phi_q(\tau)\rangle=\langle\,|\,\Phi_q\,|^2\rangle\exp(-Dq^2\tau)\ .$$

Estimating $D=K/\eta\approx10^{-5}$ cm^2/sec and probing wave vectors $q\approx10^4$ cm^{-1} and smaller yields minimum expected decay times of $\tau\approx10^{-3}$ sec and larger for Φ. Writing the mean-square orientation difference as an expansion in the Fourier modes of Φ gives

$$\sigma^2(\boldsymbol{\rho},\tau)=2\sum_q\langle\,|\,\Phi_q\,|^2\rangle(1-e^{i\mathbf{q}\cdot\boldsymbol{\rho}}e^{-Dq^2\tau})\ , \tag{13}$$

and, taking the continuum limit,

$$\sigma^2(\boldsymbol{\rho},\tau)=\frac{2k_BT}{K}\int\frac{d^2q}{4\pi^2q^2}(1-e^{i\mathbf{q}\cdot\boldsymbol{\rho}}e^{-Dq^2\tau})\ . \tag{14}$$

The ρ dependence of Eq. (14) is the same as obtained in Eq. (9) for the thin liquid-crystal slab with $K=\tilde{K}L$ and $\eta=\tilde{\eta}L$. That is, in an experiment which integrates over the orientation of Φ along the z axis the diffusive orientational dynamics of the smectic film should behave exactly as the orientational dynamics of de Gennes's hypothetical 2D nematic.

C. Logarithmic divergence

To explicitly see the logarithmic increase of σ^2 characteristic of a 2D system the integral in Eq. (14) is calculated by differentiating and integrating with respect to time:

$$\sigma^2(\boldsymbol{\rho},\tau)=\int_0^\tau dt\frac{2k_BTD}{K}\int\frac{d^2q}{4\pi^2}e^{i\mathbf{q}\cdot\boldsymbol{\rho}}e^{-Dq^2t}\ . \tag{15}$$

The q-space integral is $\pi/(4Dt)\exp(-\rho^2/4Dt)$, the Green's function of 2D diffusion.[18] Integrating this over time yields an exponential integral:[19]

$$\sigma^2(\boldsymbol{\rho},\tau)=\frac{k_BT}{\pi K}[\,A_s+\tfrac{1}{2}E_1(\rho^2/4D\tau)]\ . \tag{16}$$

A_s is the integration constant obtained from the static terms and in the case of de Gennes's model 2D nematic with $\rho\gg a$, $A_s\approx\ln\rho/a$.[16] The dynamic term $E_1(\rho^2/4D\tau)$ is an exponential integral which can be expanded:

$$E_1(x)=-\gamma-\ln(x)-\sum_{n=1}^{\infty}\frac{(-1)^nx^n}{(2n+1)!}\ , \tag{17}$$

where γ is Euler's constant $\gamma=0.577\ldots$. For $x<0.1$ the polynomial sum is negligible with respect to $\ln(x)$. For $x=\rho^2/4D\tau$ at small τ, x will necessarily be large, but for increasing τ, the regime $x<0.1$ will occur and $\ln(x)$ will dominate. In the limit $x<0.1$,

$$E_1(x)\approx-\gamma-\ln(x)=-\gamma-2\ln\rho+\ln(4D\tau)\ .$$

This logarithmic increase in σ with increasing ρ and τ is characteristic of the Landau-Peierls divergence in 2D.

The QLRO regime is that region in (ρ,τ) for which $\sigma(\rho,\tau)<1$. Solution of $\sigma(\rho,\tau)=1$ gives the time-dependent correlation range $\rho_m(\tau)$ or separation-dependent correlation time $\tau_m(\rho)$ which bound the QLRO regime. For small τ,

$$\rho_m\rightarrow\xi=a\exp(\pi K/2k_BT)$$

and for small ρ,

$$\tau_m\rightarrow\tau_m(0)=(\rho^2/4D)\exp(\pi K/2k_BT)\ .$$

The correlation parameters ξ and $\tau_m(0)$ increase extremely rapidly with decreasing temperature, with ξ becoming of the order of the size of the earth at 15 °C below the SmC-SmA transition.

III. ANALYSIS OF EXPERIMENTS

A. Experimental setup and initial observations

The experiment we report is the first cross-correlation intensity-fluctuation spectroscopy (CCIFS) study in real space. Previous CCIFS studies have involved scattering studies in reciprocal space and have been found useful for studying local anisotropies in the probed system.[20–22] The time correlation function for intensity fluctuations from two spatially separated points in the real image of the tilted smectic FSLCF is calculated. To obtain the image a polarized reflection microscope was designed using an Ar^+-ion laser as the light source. The 488.0-nm wavelength beam is spatially filtered to choose the TEM00 mode, and collimated. As Fig. 2 shows, a polarizer oriented collinearly with the laser polarization ($\vec{P}$) is in the beam path, followed by a long focal length lens and microscope objective adjusted to illuminate a 500-μm-diam region on the film with the beam's Gaussian intensity profile. The optical power density incident on the film is about 5 W/cm^2, small enough that molecular reorientations due to the electric field of the laser are negligible. Light reflected from the film passes through the same objective and part is split off by a beam splitter (50% front surface reflection, 0.05% back surface reflection). This reflected light passes through an analyzer ($\vec{A}$) crossed with respect to $\vec{P}$ and a 40-times-magnified image of this 500-μm-diam illuminated region is formed. Figure 3 is a photograph (exposure=0.1 sec) of a typical image with the average orientation field $\hat{C}(x,y)$ illustrated.

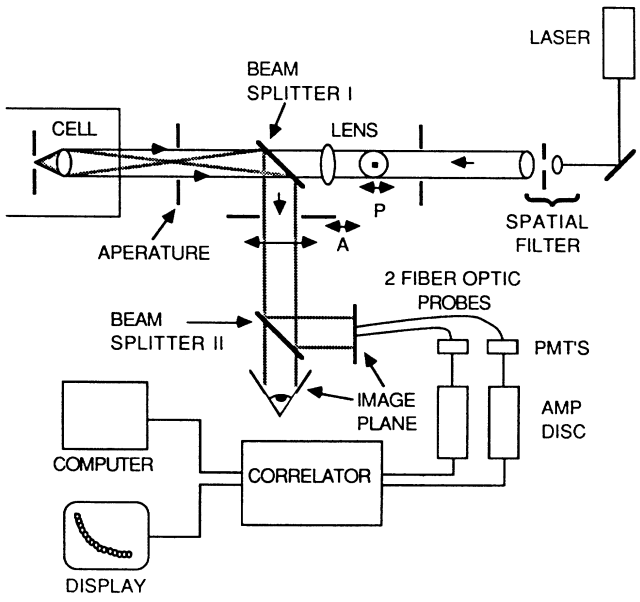

FIG. 2. The 4480-Å wavelength incident laser light is spatially filtered and collimated. It passes a vertically oriented polarizer and a long focal length achromatic lens ($F=25$ cm) and beam splitter I (BS I). The incident light split off here is dumped to the room. The light then passes through the 5× objective and onto the FSLCF. The achromat is positioned such that a 500-μm-diam region of the film is illuminated when the objective is forming an image 100 cm from the film. Half the reflected light is sent by BS I to the analyzer which passes only the light depolarized by the film. A second beam splitter BS II is placed to form two image planes. In one image plane are placed the fiber-optic probes which illuminate the PMT's. Pulse-shaping electronics collect the signals from the PMT's and send them on to the correlator, which computes the cross-correlation function. The FSLCF may be observed through an eyepiece focused on the second image plane.

The four-stage thermostat used to stabilize the FSLCF is illustrated in Fig. 4. Heaters are attached to the outermost stage and covered by a layer of aluminized Mylar, 2 cm of fiberglass insulation, and another layer of aluminized Mylar. Although the cell was designed for extremely high-precision temperature control, the temperature uniformity obtained by controlling the outermost stage to ≈ 1 mK was found to be sufficient for the experiment reported here. The millikelvin temperature control was obtained using a Handschy designed dc bridge controller.[23] The temperature near the film was found to be stable to ± 1 mK, though it was typically monitored with an electronic digital thermometer with 0.1 K sensitivity.

Adjustment of the orientation and location of the imaged portion of the FSLCF was through a series of rotation and translation stages. The cell is offset by 1-in spacers from an XY translation stage attached to a machine bed rotation table. The optical path is centered on the axis of rotation of the rotation table. By adjusting the XY translators the cell is then centered on the optical path allowing observation of the FSLCF while rotating it relative to fixed polarizer and analyzer. The inset in Fig. 4 illustrates the film holder's translation screws and springs which enable translation of the FSLCF in the optical path.

The microscopic objective used to obtain the 40-times-magnified image was a single lens 5× objective. The use of this objective introduces aberration in the image, but data are typically obtained only from the central portion of the image where the aberration is least. A higher power objective was not used since there would have been insufficient clearance for the spreader assembly to pass between objective and film holder and multiple reflections of comparable intensity as the depolarized film reflections from the additional glass-air interfaces in a multilens objective would have been introduced. The objective is focused by turning a reduction gear attached to the threaded holder. Rotation of this gear as well as the spreader and the film translation screws is by hexagonal head drivers, which are inserted from outside the cell when necessary. Using the rotation and translation stages and adjusting the microscope objective focus we were able to study any region of particular interest on the film.

The depolarized reflected intensity as a function of orientation $I(\Phi)$ is proportional to $\sin^2(2\Phi)$. In a regulated environment fluctuations in Φ are predominantly due to thermal excitation of elastically relaxed orientation variations on the continuum of lengths between molecular size and the film size. The method developed to sample the intensities at a pair of separated points in the film image is to place two 400-μm-diam monofilament fiber-optic probes in the image plane. This yields an effective resolution on the film of 12.5 μm. The intensity at each probe is measured by separate photomultipliers

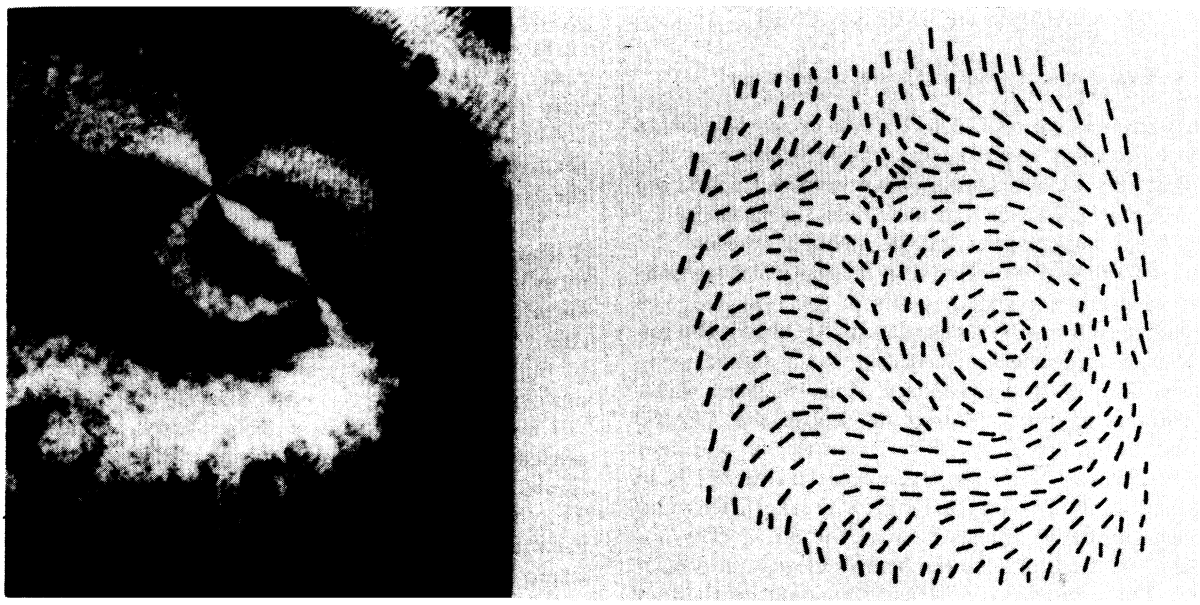

FIG. 3. A ± 1 disclination pair is illustrated. A photograph of the depolarized reflected image of a FSLCF of racemic DOBAMBC in its SmC phase illuminated with 488.0 nm light from an Ar-ion laser is shown. The film is "young" and disclination pairs formed in the spreading are still relaxing away, with this a photo of one those pairs. The film will thin to a uniform thickness and disclination pairs will annihilate, leaving a single $s = +1$ defect, within about an hour. The molecular orientation illustrating the disturbance of local order by the disclinations and the undisturbed region at the boundary is also shown.

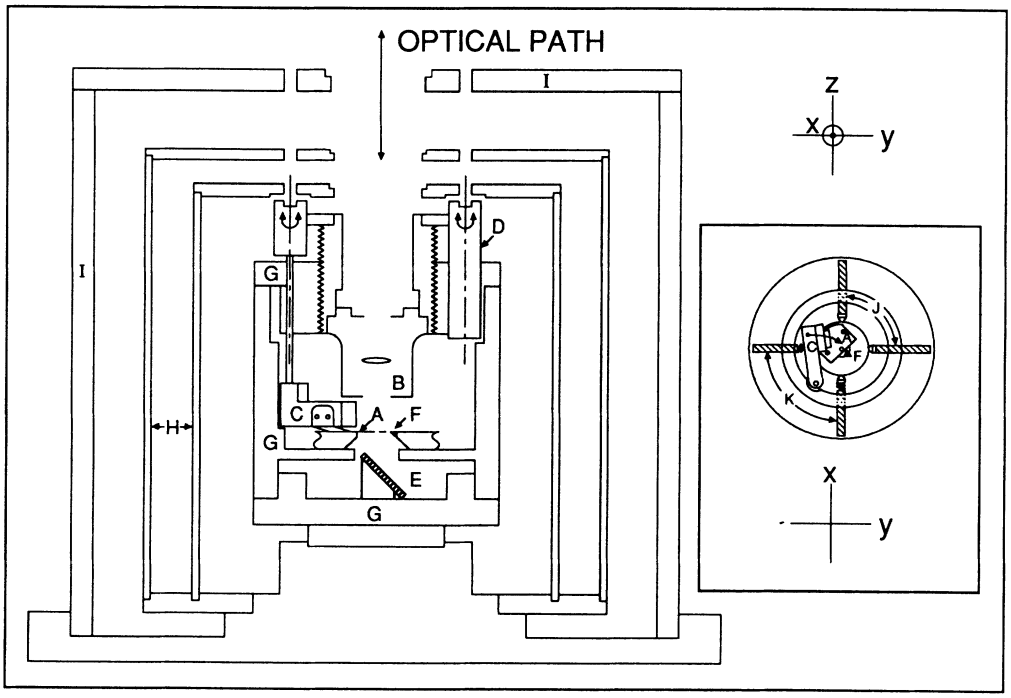

FIG 4. The sample cell is shown in cross section. The longest horizontal distance across the bottom of the cell is 6.75 in. The optical path is indicated. The FSLCF is spread across the hole in the sample holder A by sweeping the spreader C across the hole. The microscope objective B focus is adjusted by driving gear D, rotating the objective holder on its concentric threads. Light transmitted through the film reflects off the tilted black glass E and is absorbed into the walls of the black anodized interior chamber G. The black glass chip F is used as a reference reflected intensity monitor for film thickness measurements. The two interior cylindrical heat shields H are thermally connected to the outer chamber body I. Heaters are affixed to the exterior of chamber I. A circular heater is on the bottom plate, an annular heater on the top plate, and 36-gauge wire wrapped around the cylindrical body with a 1-cm pitch. Referring to the inset, a schematic top view, the sample is translated on the optical axis by rotating the drive screws J which oppose spring loaded pins K.

which provide photopulse sequences $n_1(t)$ and $n_2(t)$ to equivalent pulse-shaping electronics. These photopulse sequences are sent to the two inputs of a Langley-Ford 1096 correlator, which computes $\langle n_1(t)n_2(t+\tau)\rangle$. The line joining the fiber-optic probes may be rotated in the image plane and the distance between probe centers may be adjusted continuously between the effective fiber diameter of 12.5- and 250-μm separation. Figure 1 shows the geometry of two fiber-optic-probe faces occluding regions in the orientation field $\hat{\mathbf{C}}(x,y)$. The angle χ is the angle between ρ and the average orientation of $\hat{\mathbf{C}}(x,y)$.

The correlation function obtained is

$$R(\tau_n)=\langle n_1(t)n_2(t+\tau_n)\rangle \propto \langle I_1(t)I_2(t+\tau_n)\rangle \ . \tag{18}$$

I_1 and I_2 represent the intensities at separate points $\mathbf{r}_1$ and $\mathbf{r}_2$. $R(\tau)$ will therefore be a function of the distance $\rho=|\mathbf{r}_1-\mathbf{r}_2|$ between the two points, as well as a function of the orientation of the axis separating the probes relative to $\langle\hat{\mathbf{C}}(x,y)\rangle$, so it is appropriate to write $R(\rho,\tau_n)\propto\langle I(0,0)I(\rho,\tau_n)\rangle$, to represent the correlation function recorded. It is necessary to find the dependence of $R(\rho,\tau_n)$ on $\delta\Phi$, the fluctuations in $\Phi(x,y)$. To do this, we restrict consideration to regions in the $\sin^2(2\Phi)$ intensity profile where the intensity is on average one-half the maximum intensity. This condition may be achieved by appropriate choice of orientation of ρ relative to $\hat{\mathbf{C}}$ and maximizes $dI/d\Phi$. If the x axis is chosen along a polarizer axis, the average intensity will be half maximum at $\Phi_0=\langle\Phi\rangle=\pi/8 \pmod{\pi/4}$. To first approximation, $I(\Phi)\propto\Phi_0+\delta\Phi$, thus

$$\begin{aligned} R(\rho,\tau_n) &\propto \langle[\Phi_0+\delta\Phi(0,0)][\Phi_0+\delta\Phi(\rho,\tau_n)]\rangle \\ &\propto \langle\{\Phi_0^2+\Phi_0[\delta\Phi(0,0)+\delta\Phi(\rho,\tau_n)] \\ &\quad +\delta\Phi(0,0)\delta\Phi(\rho,\tau_n)\}\rangle \ . \end{aligned} \tag{19}$$

The thermal average of terms linear in $\delta\Phi$ is zero, that is, on average $\delta\Phi$ is symmetric about Φ_0, leaving

$$R(\rho,\tau_n)\propto\langle[\Phi_0^2+\delta\Phi(0,0)\delta\Phi(\rho,\tau_n)]\rangle \ .$$

From Eq. (12) $R\propto\sigma^2$ and thus $\sigma^2(\rho,\tau)$ may be directly studied using CCIFS. A new function $S(\rho,\tau_n)$ is defined which eliminates dependence on absolute intensity:

$$\begin{aligned} S(\rho,\tau_n) &\equiv \frac{\Xi(\rho,\tau_1,\tau_n)}{\Xi(\rho,\tau_1,\tau_N)} \\ &\equiv \frac{R(\rho,\tau_1)-R(\rho,\tau_n)}{R(\rho,\tau_1)-R(\rho,\tau_N)} \ . \end{aligned} \tag{20}$$

From Eq. (16) this yields

$$\begin{aligned} S(\rho,\tau_n) &= \frac{\sigma^2(\rho,\tau_1)-\sigma^2(\rho,\tau_n)}{\sigma^2(\rho,\tau_1)-\sigma^2(\rho,\tau_N)} \\ &= \frac{E_1\left[\frac{\rho^2}{4D\tau_1}\right]-E_1\left[\frac{\rho^2}{4D\tau_n}\right]}{E_1\left[\frac{\rho^2}{4D\tau_1}\right]-E_1\left[\frac{\rho^2}{4D\tau_N}\right]} \ , \end{aligned} \tag{21}$$

where N is the total number of time intervals in the correlation function. The function $S(\rho,\tau_n)$ is independent of the direction of ρ, characteristic of the isotropy of the 2D XY model.

Figure 5 shows two representative measurements of $S(\rho,\tau_n)$ for fixed ρ; Fig. 5(a) is a typical data set for $\chi=\pi/2$ and Fig. 5(b) is typical data for $\chi=0$. The predicted isotropy of $S(\rho,\tau_n)$ as a function of χ does not appear. For $\chi=\pi/2$, $S(\rho,\tau_n)$ is monotonic and may be fit using Eq. (21). For $\chi=0$, on the other hand, the nonmonotonic $S(\rho,\tau_n)$ shown in Fig. 5(b) cannot be obtained using Eq. (21). We found that, for the $\chi=0$ geometry, the depth of the minimum in $S(\rho,\tau_n)$ was negligible at 90 °C on all observable time scales and increases with decreasing temperature. When ρ was varied at a single temperature the scaling $\sigma^2\propto\tau$ was observed, as expected for diffusional dynamics.

The failure of the XY model to account for the $\chi=0$ data led to a variety of experiments to search for the origin of the discrepancy. The data were found to be qualitatively independent of the relative orientation of the earth's gravitational field, the density and composition of the vapor surrounding the film, or even the particular liquid crystal studied. Films of the liquid crystals $\bar{8}$S.5 and HOBACPC* have qualitatively the same anisotropic cross correlation behavior as observed in DOBAMBC. These observations indicate the anisotropy is not a peculiarity of using the mixture of both racemates of the inherently chiral DOBAMBC molecule since $\bar{8}$S.5,

$$H_{17}C_8—O—\varnothing—CH_2—S—\varnothing—C_5H_{11}$$

is not a chiral molecule, and the HOBACPC*,

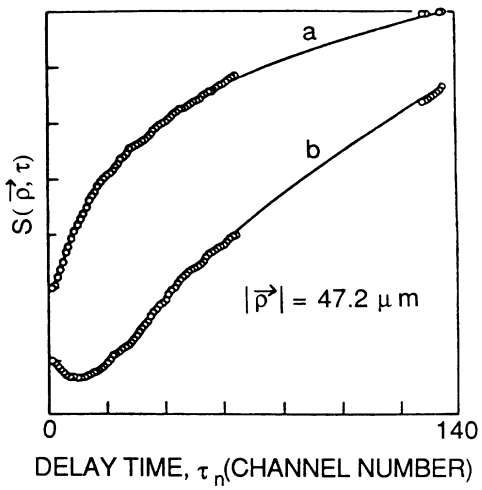

FIG. 5. These data are correlation functions scaled using Eq. (20). The last eight channels are delayed an extra 64 sample times ($64\tau_1$), and the break in the data reflects this extra delay. Plotting the data in this way causes the initial $n=1$ point and the final $n=136$ point to appear at fixed locations. The data labeled (a) are for $\chi=\pi/2$, while the data labeled (b) are for $\chi=0$. The dip in (b) reflects an anticorrelation in the intensities at the two detectors. This anticorrelation decays away being dominated by correlations at long times.

$$H_{13}C_6—O—\varnothing—CH=N—\varnothing—CH=CH—CO—O—CH_2—(CHClCH_3)$$

used was dominated by the left-handed enantiomorph.

B. Outline of theoretical analysis

To assist in understanding the information contained in the observed cross-correlation functions the following points are emphasized. (i) The XY model predicts that the decay of the cross-correlation function will be logarithmic in time. Usual methods of correlation-function analysis of dynamic scattering involve obtaining single- or multiexponential relaxation to some finite background. Inherent in a logarithmic time decay is the absence of a background cutoff and scaling with time. In addition, fluctuations of wavelength shorter than the probe size are averaged, providing a short-time cutoff. (ii) The finite sample size limits the smallest wave vector which may affect $S(\rho,\tau_n)$, introducing a cutoff with a characteristic time of 50 to 5000 sec depending on D, so that there is a background on a very long time scale. (iii) Since we are probing the cross correlation of intensities between regions in real space rather than points, a resolution function associated with finite probe size must be folded with the $I(\Phi)$ dependence (discussed in Sec. III C). (iv) To calculate $R(\rho,\tau_n)$ used in Eq. (20) we assumed $I(\Phi) \propto \Phi_0+\delta\Phi$. We will show that to account for the anticorrelation exhibited in Fig. 5(b) it is necessary to include terms to order $(\delta\Phi)^3$ in the $I(\Phi)$ proportionality (discussed in Sec. III D). (v) The data presented in Fig. 5 clearly show anisotropy as a function of χ. This anisotropy is explained by the anisotropic elastic constants for splay and bend in 2D previously observed in smectic films and requires that the 2D XY model be modified to describe our data (discussed in Sec. III E). (vi) At long enough times that $x=\rho^2/4Dt<0.1$, the exponential integral in Eq. (21) will exhibit the logarithmically increasing time dependence characteristic of the Landau-Peierls divergence. This logarithmic divergence is observed at very long times independent of spatial separation (data are presented in Sec. IV A). Items (iii), (iv), and (v) discussed above only significantly modify the shape of the observed cross-correlation function from that predicted by Eq. (21), in the ρ,τ regime $x>0.1$.

C. Finite probe size

For $|\rho|$ significantly larger than the fiber-optic-probe diameter, Eq. (21) seems to fit the data for $\chi=\pi/2$ perfectly, when the fitting parameter D is allowed to vary. For $|\rho|$ comparable to the probe diameter the decay of $S(\rho,\tau_n)$ deviates from the calculated dependence even for $\chi=\pi/2$. This deviation is due to the finite size of the probes. The calculation of $\sigma^2(\rho,\tau)$ in Eq. (16) was based on orientation correlations between two points. The fiber-optic probes occlude regions of nonzero area rather than points, therefore a resolution function cutting off the integration at large wave vector should be folded into the integration in Eq. (14). For simplicity of calculation assume that the light transmitted by the probes has a Gaussian intensity profile about the center of the probes. Then the transmitted intensity is proportional to $\exp(2\pi r^2/\alpha)$, where α depends on the cross-sectional area of the fiber. The probe profile is accounted for by including the factor $\exp(-\alpha q^2)$ in the integrand of Eq. (14). This manifests itself in the argument of the exponential integral included in Eq. (16) as follows:

$$\sigma^2(\rho,\tau)=\frac{k_BT}{\pi K}\{A_s+\tfrac{1}{2}E_1[\rho^2/4(D\tau+\alpha)]\} . \tag{22}$$

The arguments of all four exponential integrals in Eq. (21) are modified by the addition of this finite-probe-size contribution. This is effectively a constant displacement along the time axis due to the shortest time (largest wave vector) fluctuations averaged over by the probes. We find that fits with $\alpha=36\ \mu m^2$ work well as an empirical correction for all data.

D. Anticorrelation

The time correlation of a random process as probed by photon spectroscopy decays from $\langle n_i^2\rangle$ to $\langle n_i\rangle^2$, where n_i is the number of photons detected in the ith time interval and the average is taken over many intervals. By the triangle inequality $\langle n_i^2\rangle>\langle n_i\rangle^2$, therefore an autocorrelation function may not exhibit data which behave as that shown in Fig. 5(b). Anticorrelation is defined as an increase with time of a cross-correlation function $\langle n_in_j\rangle$.

At least two CCIFS experiments reporting anticorrelation are in the literature. (1) Clark, Ackerson, and Hurd[22] and Ruth, Clark, and Ackerson[24] have reported the detection of an anticorrelation in a monolayer colloidal solution near the order-disorder transition, in which the correlation coefficient decays up to its background value with time. (2) Griffin and Pusey have reported cross-correlation data very similar in appearance to that shown in Fig. 5(b).[20] Their experiment involved cross correlating the scattering from a dilute solution of tobacco mosaic virus at $\pi/2$ and $3\pi/2$ rad relative to the incident laser direction. Anticorrelation was due to differential interference of the scattering from the anisotropic particles at the two detectors.

The anticorrelation observed here is a consequence of the small elastic-restoring forces in this 2D system allowing large-amplitude orientation fluctuations. Rosenblatt *et al.* found values for K_S and K_B for a three-layer film of DOBAMBC.[7,25] The values found increased linearly with decreasing temperature from the SmC-SmA phase transition and are fit to within experimental error by

$$\begin{aligned} K_S&=1.12\times10^{-13}(T^*-T)\ \text{erg/K} ,\\ K_B&=1.52\times10^{-14}(T^*-T)\ \text{erg/K} , \end{aligned} \tag{23}$$

where T ranges from 90 to 115 °C in the SmC phase below T^* (for splay $T^*=116$ °C, for bend $T^*=118.5$ °C). T^* is not the SmA-SmC phase transition temperature in the FSLCF, $T_{CA}\approx115$ °C, because there is a discontinuity in the linear decrease of both elastic constants very close to the transition (the transition is weakly first order). If these values are assumed to represent indepen-

dent elastic constants for splay and bend fluctuations in $\hat{C}(x,y)$, the resulting predicted values for $\sigma^2(\rho,\tau)$ are anisotropic. For the experimentally accessible regimes, σ is calculated to range up to about 7° for the splay case and about 20° for the bend case. The $S(\rho,\tau_n)$ dependence on $\delta\Phi$ leading to Eq. (21) was based on $I(\Phi)$ fluctuating only linearly in $\delta\Phi$. Since $I(\Phi)\propto\sin^2(2\Phi)$, for $\Phi_0=\pi/8$ and the average bend fluctuation of 20°, it is necessary to include terms to third order in $\delta\Phi$. The linear approximation should be more accurate for the average splay fluctuation.

To understand the anticorrelation we will expand the depolarized reflected electric field of the laser $E(\Phi)$ in a Taylor series about an average director orientation Φ_0, including terms to fourth order in fluctuations about that average. We then calculate the intensity $E(\Phi)E^*(\Phi)$ to fourth order and simplify for our geometry. There are two nonzero contributions to $S(\rho,\tau_n)$, the linear-linear

$$\delta\Phi\,\delta\Phi\equiv\langle\{\delta\Phi(0,0)[\delta\Phi(\rho,\tau_1)-\delta\Phi(\rho,\tau_n)]\}\rangle$$

terms which led to Eq. (21) and linear-cubic ($\delta\Phi\,\delta\Phi^3$ defined subsequently) terms, the inclusion of which explains the observed anticorrelation. We obtain $\Xi(\rho,\tau_1,\tau_n)$ and substitute this result into $S(\rho,\tau_n)$ in Eq. (21). Good fits to the data may be obtained by varying both the diffusion constant D and the elastic constant K. The diffusion constants obtained from these fits consistently vary by a factor of 6 or 7 when χ is varied from 0 to $\pi/2$. This is consistent with the splay-bend anisotropy in elastic constants observed by Rosenblatt (discussion in Sec. III E).

A Taylor expansion of the depolarized reflected electric field $E(\Phi)=E_0\sin2\Phi$ around some Φ_0 gives, to fourth order in $\delta\Phi$:

$$E(\Phi)=E_0[\sin(2\Phi_0)+2(\delta\Phi)\cos(2\Phi_0)-2(\delta\Phi)^2\sin(2\Phi_0)-\tfrac{4}{3}(\delta\Phi)^3\cos(2\Phi_0)+\tfrac{2}{3}(\delta\Phi)^4\sin(2\Phi_0)]\ . \quad (24)$$

Squaring $E(\Phi)$ to obtain $I(\Phi)$ to fourth order in $\delta\Phi$ and simplifying gives

$$\frac{I(\Phi)}{E_0^2}=\sin^2(2\Phi_0)+2(\delta\Phi)\sin(4\Phi_0)+4(\delta\Phi)^2\cos(4\Phi_0)-\tfrac{16}{3}(\delta\Phi)^3\sin(4\Phi_0)-\tfrac{16}{3}(\delta\Phi)^4\cos(4\Phi_0)\ . \quad (25)$$

The correlation function developed in the lab is $\langle I(0,0)I(\rho,\tau)\rangle$, which we now calculate to fourth order in $\delta\Phi$, realizing that the thermal average of any term of odd order in $\delta\Phi$ is zero. The film may be translated and rotated in the (X,Y) plane allowing choice of any Φ_0. Three limiting cases exist $\Phi_0=0$ mod $\pi/2$, $\Phi_0=\pi/8$ mod $\pi/4$, and $\Phi_0=\pi/4$ mod $\pi/2$. For $\Phi_0=0$ (the middle of a dark brush, $I_{\rm ave}=I_{\rm min}$) terms with $\sin^2\Phi_0$ or $\sin^4\Phi_0$ as a factor are zero, and the first two nonzero terms are fourth and sixth order in $\delta\Phi$. For $\Phi_0=\pi/4$ (the middle of a bright region, $I_{\rm ave}=I_{\rm max}$) terms with $\sin^4\Phi_0$ as a factor are zero. The cross-correlation function has the same fourth- and sixth-order terms as for the $\Phi_0=0$ case, as well as terms of the form $\langle\delta\Phi^2\rangle$ and $\langle\delta\Phi^4\rangle$. Since $\delta\Phi$ is assumed to be a stationary random variable, $\langle\delta\Phi^2\rangle$ and $\langle\delta\Phi^4\rangle$ are constants. Fluctuations in the brightest region and in the darkest region are given by the same averages, but with different relative amplitudes. For $\Phi_0=\pi/8$ (between a bright and dark region, $I_{\rm ave}=\frac{1}{2}I_{\rm max}$) terms with $\cos^4\Phi_0$ as a factor are zero, therefore to fourth order:

$$\frac{1}{E_0^4}\langle I(0,0)I(\rho,\tau)\rangle=\tfrac{1}{4}+4\langle\delta\Phi(0,0)\delta\Phi(\rho,\tau)\rangle-\tfrac{32}{3}\langle\{\delta\Phi(0,0)[\delta\Phi(\rho,\tau)]^3+[\delta\Phi(0,0)]^3\delta\Phi(\rho,\tau)\}\rangle\ . \quad (26)$$

The data presented here were taken in the $\Phi_0=\pi/8$ region. $\Xi(\rho,\tau_1,\tau_n)$ contains the only time-dependent terms of $S(\rho,\tau_n)$ and to fourth order in $\delta\Phi$ becomes

$$\Xi(\rho,\tau_1,\tau_n)\propto\langle\delta\Phi(0,0)[\delta\Phi(\rho,\tau_1)-\delta\Phi(\rho,\tau_n)]\rangle-\tfrac{8}{3}\langle\delta\Phi(0,0)\{[\delta\Phi(\rho,\tau_1)]^3-[\delta\Phi(\rho,\tau_n)]^3\}+[\delta\Phi(0,0)]^3[\delta\Phi(\rho,\tau_1)-\delta\Phi(\rho,\tau_n)]\rangle\ . \quad (27)$$

The quartic terms in Eq. (27) define the $\delta\Phi(\delta\Phi)^3$ terms. The $\delta\Phi\,\delta\Phi$ term is the term which leads to the exponential integral dependence for $S(\rho,\tau_n)$ in Eq. (21). As an example of the type of term obtained from the quartic contribution $\langle\delta\Phi(0,0)[\delta\Phi(\rho,\tau)]^3\rangle$ will be calculated in the one elastic constant approximation and $S(\rho,\tau_n)$ will then be presented. Fourier expanding this fourth-order term and integrating over all wave vectors gives

$$\langle\delta\Phi(0,0)[\delta\Phi(\rho,\tau)]^3\rangle=\frac{1}{(2\pi)^8}\int d^2q_1\int d^2q_2\int d^2q_3\int d^2q_4\langle\Phi_{q_1}\Phi_{q_2}\Phi_{q_3}\Phi_{q_4}\rangle e^{i(q_2+q_3+q_4)\cdot\rho}e^{-D(q_2^2+q_3^2+q_4^2)\tau}\ . \quad (28)$$

Note that the $\langle\delta\Phi(\rho,\tau)[\delta\Phi(0,0)]^3\rangle$ term is similar to Eq. (28) but the exponentials contain only the wave vector q_1. The thermal average of the Fourier coefficients in Eq. (28) is zero except when the coefficients form conjugate pairs and $\langle|\Phi_q|^2\rangle=k_BT/Kq^2$, leaving a simpler integration over two variables:

$$\langle\delta\Phi(0,0)[\delta\Phi(\rho,\tau)]^3\rangle=\frac{3(k_BT)^2}{(2\pi)^4K^2}\int\frac{d^2q_1}{q_1^2}e^{iq_1\cdot\rho}e^{-Dq_1^2\tau}\int\frac{d^2q_2}{q_2^2}e^{-2Dq_2^2\tau}\ . \quad (29)$$

The integral over q_1 yields $A_s+\frac{1}{2}E_1(\rho^2/4D\tau)$. The integral over q^2 may easily be manipulated into the basic form of

the exponential integral and yields $E_1(2Dq_m^2\tau)-E_1(2Dq_x^2\tau)$, where q_m and q_x are, respectively, the minimum and maximum wave vectors probed in the experiment. The maximum wave vector probed is associated with the area occluded by the detector, which corresponds to a diameter on the film of $d\approx 12.5$ μm. Therefore, $q_x=2\pi/12.5$ μm≈ 4500 cm^{-1} is chosen. The minimum wave vector probed is associated with the time the experiment was allowed to run, decreasing with increasing run time until it is cut off by the size of the sample, resulting in $q_m\approx 10-100$ cm^{-1}. Integrating with these limits yields

$$\langle \delta\Phi(0,0)[\delta\Phi(\rho,\tau)]^3\rangle = \frac{3(k_BT)^2}{(2\pi)^4K^2}[A_s+\tfrac{1}{2}E_1(\rho^2/4D\tau)][E_1(2Dq_m^2\tau)-E_1(2Dq_x^2\tau)] . \tag{30}$$

The $\langle[\delta\Phi(0,0)]^3\delta\Phi(\rho,\tau)\rangle$ term is calculated similarly, yielding the same expression except that the difference in exponential integrals in Eq. (30) is replaced by $\ln(q_x/q_m)$. Including terms to fourth order in $\delta\Phi$ for $\Phi_0=\pi/8$ in $\Xi(\rho,\tau_1,\tau_n)$ yields

$$\Xi(\rho,\tau_1,\tau_n)\propto Q_n-Q_1-A_4(C_1-C_2-C_3+C_4) , \tag{31}$$

where

$$Q_n\equiv E_1(\rho^2/4D\tau_n) , \quad A_4=\frac{4k_BT}{\pi K} ,$$
$$C_1=A_s[E_1(2Dq_m^2\tau_1)-E_1(2Dq_x^2\tau_1)] ,$$
$$C_2=Q_1[E_1(2Dq_m^2\tau_1)-E_1(2Dq_x^2\tau_1)-\ln q_m+\ln q_x] ,$$
$$C_3=A_2[E_1(2Dq_m^2\tau_n)-E_1(2Dq_x^2\tau_n)] ,$$
$$C_4=Q_n[E_1(2Dq_m^2\tau_n)-E_1(2Dq_x^2\tau_n)-\ln q_m+\ln q_x] .$$

Equation (31) includes the functional dependence necessary to qualitatively explain the anticorrelation observed. The first two terms Q_1 and Q_n are the second-order terms which appear in Eq. (21). The leading factor for the fourth-order terms A_4 depends inversely on the effective orientational elastic constant probed. Recall that Rosenblatt *et al.* found $K_S\approx 7K_B$ [Eq. (23)], therefore a geometry in which the experiment probed only bend fluctuations would have almost an order of magnitude larger fourth-order contribution than the corresponding splay geometry. A comparison of the relative magnitudes of the $\delta\Phi(\delta\Phi)^3$ terms shows that the terms involving $E_1(2D\tau q_x^2)$ are negligible by many orders of magnitude with respect to the corresponding terms involving $E_1(2D\tau q_m^2)$. The terms involving $\ln(q_x/q_m)$ arise from the $[\delta\Phi(0,0)]^3\delta\Phi(\rho,\tau)$ term and range from 4% to 6% of the $\delta\Phi\,\delta\Phi$ terms, depending on the magnitude of q_m. The finite probe size effects have been ignored in this calculation of $\Xi(\rho,\tau_1,\tau_n)$.

An accurate determination of the integration constant A_s is required to determine the relative magnitudes of the $\delta\Phi\,\delta\Phi$ and the $\delta\Phi(\delta\Phi)^3$ terms. The determination of A_s is somewhat subtle. It arises in the integration over q_1 in Eq. (29) and may not be approximated by $\ln(\rho/a)$ as in Eq. (16). When differentiated and integrated from 0 to τ, the q_1 integration becomes

$$\int \frac{d^2q_1}{q_1^2}e^{iq_1\cdot\rho}e^{-D^2q_1\tau} = A_s+\int_0^\tau dt\int d^2q_1-De^{iq_1\cdot\rho}e^{-D^2q_1\tau} , \tag{32}$$

where $A_s=\int d^2q/q^2\exp(i\mathbf{q}\cdot\boldsymbol{\rho})$. Including the finite probe size Gaussian contribution and integrating A_s over the angular coordinate yields

$$A_s=2\pi\int_{q_m}^{q_x}dq\frac{1}{q}J_0(q\rho)e^{-\alpha q^2} , \tag{33}$$

which must be integrated from the minimum to maximum wave vector numerically. The effects of including $\exp(-\alpha q^2)$ in this development are to modify the arguments of the exponential integrals:

$$E_1(\rho^2/4D\tau)\longrightarrow E_1[\rho^2/4(D\tau+\alpha)] ,$$
$$E_1(2Dq^2\tau)\longrightarrow E_1[(2D\tau+\alpha)q^2] . \tag{34}$$

We may now attempt to fit the data using Eq. (31) with the arguments of the exponential integrals so modified. In order to fit the data we must determine q_m, α, A_s, A_4, and D. The other quantities (ρ,τ_n) are determined by the instrumentation. The minimum wave vector probed q_m is chosen as $(\pi^3/Dt_{\rm run})^{1/2}$ or 10 cm^{-1}, whichever is larger, to reflect the decrease in the minimum wave vector probed with increasing run time until a cutoff associated with the finite-system size is reached. The choice of α is made as discussed in Sec. III C and is unchanged for fitting all the data ($\alpha=3.6\times 10^{-7}$ cm^2). The value of A_s is determined by numerical integration of Eq. (33), with the same choice of minimum wave vector as just discussed and maximum wave vector chosen associated with the detector size. The temperature is monitored using a thermistor near the sample connected to a digital thermistor thermometer which displays the absolute temperature ± 0.1 °C. The effective elastic constant is unknown, though an estimate of the magnitude is possible from Eq. (23). $A_4(K)$ is allowed to vary for best fit, as is the diffusion constant D. If these two parameters are allowed to vary freely, good fits to all the data may be obtained. For $\chi=0$ the best fit to the data is sensitive to variation of K by about 50%. The fit to the data is most sensitive to choice of diffusion constant D and in allowing variation for best fit we may determine D to about 10% for all geometries.

Using Eq. (31) with the finite probe size modifications of Eq. (34) both monotonic and nonmonotonic data may be fit well. This model was obtained upon realizing that the large amplitude of the fluctuations causes the probed intensity to vary nonlinearly. Bend fluctuations are large enough to exhibit this nonlinearity. The anisotropy in the orientational dynamics is related to the elastic constant anisotropy, and we now explore this anisotropy in detail.

E. Anisotropic elastic constants

To understand the significance of the values of D and K obtained by fitting the data, we must consider the modifications to our model needed to account for the anisotropy in elastic constants. The orientational elastic free energy of a 2D nematic is given in Eq. (3). Recalling that $\Phi(x,y)$ is the orientation of $\hat{\mathbf{C}}(x,y)$ relative to the x axis we expand this free energy in x and y coordinates:

$$F-F_0=\left[\frac{K_S}{2}\left[\frac{\partial\cos\Phi}{\partial x}+\frac{\partial\sin\Phi}{\partial y}\right]^2+\frac{K_B}{2}\left[\frac{\partial\sin\Phi}{\partial x}-\frac{\partial\cos\Phi}{\partial y}\right]^2\right]. \tag{35}$$

Choosing the x axis along $\langle\Phi\rangle=\Phi_0$ and expanding $\partial\Phi/\partial x$ and $\partial\Phi/\partial y$ in their Fourier components gives the energy per mode $\langle|\Phi_q|^2\rangle=k_BT/(K_Bq_x^2+K_Sq_y^2)$. The contribution to $\Xi(\rho,\tau_1,\tau_n)$ due to the $\delta\Phi\,\delta\Phi$ terms with $K_S\neq K_B$ will now be calculated to illustrate the approximations required to deal with this anisotropy. The dynamics of these linear terms are given by

$$\langle\Phi_{-q}(0)\Phi_q(\tau)\rangle=\langle|\Phi_q(0)|^2\rangle\exp[-D(q)q^2\tau]\,.$$

In general we may write

$$D(q)q^2=D_Bq_x^2+D_Sq_y^2$$

and the dynamic contribution becomes

$$\exp[-(D_Bq_x^2+D_Sq_y^2)\tau]\,.$$

Thus the $\delta\Phi\,\delta\Phi$ contribution to $\Xi(\rho,\tau_1,\tau_n)$ becomes

$$\delta\Phi\,\delta\Phi=\sum_q\frac{k_BT}{K_Bq_x^2+K_Sq_y^2}e^{i\mathbf{q}\cdot\rho}\times(e^{-(D_Bq_x+D_S^2q_y)\tau_1^2}-e^{-(D_Bq_x+D_S^2q_y)\tau_n^2})\,. \tag{36}$$

In the continuum limit and differentiating and integrating with respect to time,

$$\delta\Phi\,\delta\Phi=\int_{\tau_n}^{\tau_1}dt\frac{k_BT}{4\pi^2}\int dq_x\int dq_y\frac{(D_Bq_x^2+D_Sq_y^2)}{(K_Bq_x^2+K_Sq_y^2)}e^{i\mathbf{q}\cdot\rho}e^{-(D_Bq_x^2+D_Sq_y^2)\tau_1}\,. \tag{37}$$

The integrals over q_x and q_y in Eq. (37) are not obtainable in analytic form in general. The diffusion constants are, in general, $D(q)=K(q)/\eta(q)$. The functional dependence of $K(q)$ is a splitting into independent splay and bend relaxational modes with a large anisotropy in energy. The functional dependence exhibited by $\eta(q)$ is much less anisotropic, with Rosenblatt measuring about a 5% difference in the magnitudes of η_S and η_B, and qualitatively the same temperature dependence. If the approximation $\eta=\eta_S=\eta_B$ is made, the integrations over q_x and q_y separate resulting in

$$\delta\Phi\,\delta\Phi=\int_{\tau_1}^{\tau_n}dt\frac{k_BT}{2\pi\eta t\sqrt{D_BD_S}}\times\exp\left[\frac{-1}{4t}\left[\frac{\rho_x^2}{D_B}+\frac{\rho_y^2}{D_S}\right]\right]. \tag{38}$$

The time integral may now be done, it being a form of the exponential integral. The correct point-point correlation function involving terms linear in the orientation fluctuations, with $K_S\neq K_B$ is

$$\delta\Phi\,\delta\Phi=\frac{k_BT}{2\pi\sqrt{K_BK_S}}\left\{E_1\left[\frac{1}{4\tau_1}\left[\frac{\rho_x^2}{D_B}+\frac{\rho_y^2}{D_S}\right]\right]-E_1\left[\frac{1}{4\tau_n}\left[\frac{\rho_x^2}{D_B}+\frac{\rho_y^2}{D_S}\right]\right]\right\}. \tag{39}$$

In the case that either ρ_x or ρ_y is zero [for the probes separated perpendicular or parallel to the average orientation of $\hat{\mathbf{C}}(x,y)$] the only modification to the one constant approximation is the replacement of K by $(K_SK_B)^{1/2}$.

Since the probes are symmetric in X and Y while the fluctuations are not, including $\exp(-\alpha q^2)$ terms in Eq. (36) changes terms of the form Dt in Eq. (38) to $Dt+\alpha$. Then, even for ρ_x or ρ_y equal to zero, the time integration is not analytic. Numerical integration is possible though. Choosing either ρ_x or ρ_y equal to zero, Eq. (38) becomes

$$\delta\Phi\,\delta\Phi=\frac{k_BT}{2\pi\eta}\int_{\tau_n}^{\tau_1}dt\frac{1}{\sqrt{Dt+\alpha}\sqrt{D't+\alpha}}\times\exp[-\rho^2/4(Dt+\alpha)]\,, \tag{40}$$

where there exist (i) the bend case $\rho=\rho_x$, $D=D_B$, $D'=D_S$, and (ii) the splay case $\rho=\rho_y$, $D=D_S$, and $D'=D_B$. Substituting $p=(Dt+\alpha)^{-1}$, Eq. (40) is amenable to numerical integration:

$$\delta\Phi\,\delta\Phi=\frac{k_BT}{2\pi\sqrt{K_SK_B}}\int_{p_1}^{p_n}\frac{dp}{p}\exp(-\rho^2p/4)\times\left[1+p\alpha\left[\frac{D}{D'}-1\right]\right]^{1/2}, \tag{41}$$

where $p_n=(D\tau_n+\alpha)^{-1}$. Note, if $\alpha=0$, Eq. (41) is equivalent to Eq. (39) with ρ_x or ρ_y equal to zero. Considering finite probe size ($\alpha\neq0$) in the square root in (41)

requires increasing D_S for best fit in the splay case, and reducing D_B for best fit in the bend case. This is exemplified in Fig. 6, where

$$\frac{\delta\Phi_1\delta\Phi_n}{\delta\Phi_1\delta\Phi_N}=\frac{\langle\delta\Phi(\mathbf{0},0)[\delta\Phi(\boldsymbol{\rho},\tau_1)-\delta\Phi(\boldsymbol{\rho},\tau_n)]\rangle}{\langle\delta\Phi(\mathbf{0},0)[\delta\Phi(\boldsymbol{\rho},\tau_1)-\delta\Phi(\boldsymbol{\rho},\tau_N)]\rangle} \tag{42}$$

is calculated by numerical integration (using a simple trapezoidal method), for the three cases: (1) the splay case, $D=D_S$, $D'=D_B=D_S/7$; (2) the bend case $D=D_B$, $D'=D_S=7D_B$; and (3) the one constant approximation $DD'=D_SD_B$, with the $p\alpha$ term in the square root absent. Also plotted in Fig. 6(a) is the curve for $\delta\Phi_1\delta\Phi_n$ as calculated in Eq. (39) for $\alpha=0$. The arbitrary choice of $D=2.3\times10^{-5}$ cm^2/sec was made for all three cases plotted. The integral in Eq. (41) may be scaled by any constant and the calculation of Eq. (42) will be unchanged. The separation of the $\alpha\neq0$ curves plotted is due to fluctuations perpendicular to ρ mixing with the fluctuations parallel to ρ. For the $\alpha\neq0$ cases shown in Fig. 6(a) $\rho=20$ μm and the initial slope in all three cases is much larger than for the $\alpha=0$ case. This may be interpreted as an averaging over the short-time fluctuations of wavelength smaller than the probe diameter. Because τ scales as ρ^2, for probe separations as large as a few times probe diameter the effect of including $\exp(-\alpha q^2)$ becomes insignificant. For $\rho=50$ μm [shown in Fig. 6(b)] the separation of the three curves exemplifies the decreasing influence of probe size.

To understand the values for the diffusion constants obtained from best fit of the data we must calculate

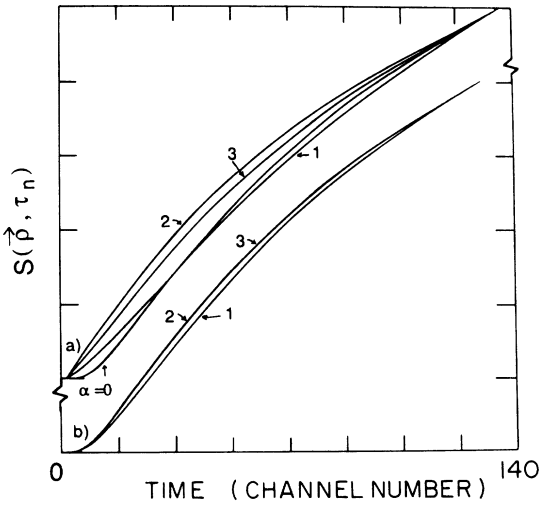

FIG. 6. The effect of including the circular probe profile in the calculation of the second-order contribution to $S(\rho,\tau_n)$ using anisotropic elastic constants is illustrated. The quantity $\delta\Phi_1\delta\Phi_n/\delta\Phi_1\delta\Phi_N$ as expressed in Eq. (42) is calculated for two choices of ρ and τ_1, (a) for $\rho=20$ μm, $\tau_1=1.8$ msec and (b) $\rho=50$ μm, $\tau_1=11$ msec. For $\rho=20$ μm the point-point cross correlation is shown (labeled $\alpha=0$). For both (a) and (b) the three cases (1) splay, (2) bend, and (3) the one constant approximation are calculated and shown.

$\Xi(\rho,\tau_1,\tau_n)$ to fourth order in $\delta\Phi$ for the case of anisotropic elastic constants and including the probe profile. The $\delta\Phi\,\delta\Phi$ terms are shown in Eq. (41). The general expression for the $\delta\Phi(\delta\Phi)^3$ contribution is

$$\langle\delta\Phi(\mathbf{0},t_1)[\delta\Phi(\boldsymbol{\rho},t_2)]^3\rangle=\frac{3}{4\pi^2}\int d^2q_1\frac{k_BT}{K_Bq_{1x}^2+K_Sq_{1y}^2}e^{i\mathbf{q}_1\cdot\boldsymbol{\rho}}(e^{-\alpha q_1^2}e^{-(t_1+t_2)(D_Bq_{1x}^2+D_Sq_{1y}^2)})$$
$$\times\int d^2q_2\frac{k_BT}{K_Bq_{2x}^2+K_Sq_{2y}^2}e^{i\mathbf{q}_2\cdot\boldsymbol{\rho}}e^{-\alpha q_2^2}e^{-2t_2(D_Bq_{2x}^2+D_Sq_{2y}^2)}, \tag{43}$$

where there are two cases: (i) $t_1=0$, $t_2=\tau$ and (ii) $t_1=\tau$, $t_2=0$. For both cases the integration over q_1 yields a term

$$A_s-\frac{\sqrt{K_BK_S}}{4\pi^2k_BT}\delta\Phi\,\delta\Phi\,, \tag{44}$$

where the $\delta\Phi\,\delta\Phi$ term is that shown in Eq. (41) with limits of integration from $p_n=(D\tau+\alpha)^{-1}$ to $p_1=1/\alpha$. Integration over q_2 in polar coordinates yields the term

$$\frac{k_BT}{2}\int_0^{2\pi}d\theta\frac{E_1(\Lambda q_m^2)-E_1(\Lambda q_x^2)}{K_B\cos^2\theta+K_S\sin^2\theta}\,, \tag{45}$$

with Λ different for the two cases. For case (i)

$$\Lambda=\alpha+2\tau(D_B\cos^2\theta+D_S\sin^2\theta)\,,$$

while for case (ii) $\Lambda=\alpha$. For case (ii) the angular integration is analytic while for case (i) the θ dependence in the argument of the exponential integral prevents an analytic solution. Realizing that only a small error is made, we replace $(D_B\cos^2\theta+D_S\sin^2\theta)$ in Λ with $(D_BD_S)^{1/2}$, obtaining a tractable expression for the integration. This substitution replaces the elliptical limits of integration at minimum wave vector with circular limits of radius $(D_BD_S)^{1/2}$. This is justifiable when the integrand is near 1 at the minimum wave vector, which is indeed true for our experiment. The contribution to the $\delta\Phi(\delta\Phi)^3$ terms for the integration over q_2 are terms of the form

$$\frac{8k_BT}{\sqrt{K_BK_S}}\arctan\left[\frac{K_S}{K_B}\right]^{1/2}[E_1(\Lambda q_m^2)-E_1(\Lambda q_x^2)]\,. \tag{46}$$

Incorporating the results necessary for a detailed understanding of data fits [from Eqs. (41), (43), (45), and (46)] we find the final form of $\Xi(\rho,\tau_1,\tau_n)$:

$$\Xi(\rho,\tau_1,\tau_n)\propto Q_n-Q_1-A_4(C_1-C_2-C_3+C_4)\,, \tag{47}$$

where

$$Q_n \equiv \int_{(1/D\tau+\alpha)}^{1/\alpha} \frac{dp}{p} e^{-\rho^2/4}\left[1+p\alpha\left[\frac{D}{D'}-1\right]\right],$$

$$A_4 = \frac{4k_BT}{\pi\sqrt{K_BK_S}}\arctan\left[\frac{K_S}{K_B}\right]^{1/2},$$

$$C_1 = A_s[E_1(q_m^2\Lambda_1)-E_1(q_x^2\Lambda_1)],$$

$$C_2 = Q_1[E_1(q_m^2\Lambda_1)-E_1(q_x^2\Lambda_1)+E_1(q_m^2\alpha)-E_1(q_x^2\alpha)],$$

$$C_3 = A_s[E_1(q_m^2\Lambda_n)-E_1(q_x^2\Lambda_n)],$$

$$C_4 = Q_n[E_1(q_m^2\Lambda_n)-E_1(q_x^2\Lambda_n)+E_1(q_m^2\alpha)-E_1(q_x^2\alpha)],$$

$$A_s = \int \frac{dq}{q} J_0(q\rho)e^{-\alpha q^2},$$

$$\Lambda_n \equiv \alpha + 2\tau_n\sqrt{D_SD_B}\ .$$

Using Eq. (47) to obtain

$$S(\boldsymbol{\rho},\tau_n) = \Xi(\boldsymbol{\rho},\tau_1,\tau_n)/\Xi(\boldsymbol{\rho},\tau_1,\tau_N)$$

we are able to fit the data by using values for K_S and K_B extrapolated from Rosenblatt's data and obtain very reasonable consistency in the determination of the diffusion constants. Note that in spite of its rather complicated appearance, Eq. (47) is still a two-parameter fit involving the appropriate splay or bend elastic and diffusion constants. As mentioned previously the best fit to the data is sensitive to change in K of 50% and change in D of 10%. These uncertainties remain when Eq. (47) is used to fit the data. The additional understanding we have achieved in calculating Eq. (47) is accurate determination of D_S and D_B. Compared with those values obtained using the one constant approximation, the best-fit diffusion constant for the splay case increases about 15% for small values of $|\boldsymbol{\rho}|$. For the bend case at small $|\boldsymbol{\rho}|$ the best-fit D_B decreases about 50%. We believe that Eq. (47) enables determination of D_S and D_B independently for an arbitrary choice of $\boldsymbol{\rho}$ and τ. We now present data illustrating these points.

IV. EXPERIMENTAL RESULTS

A. Temporal variation

The original aim of this work was to study the dynamics of a real two-dimensional orientation field in the QLRO regime. The ubiquitous feature of a system exhibiting the Landau-Peierls instability in the QLRO regime is a logarithmic divergence of order in both space and time. The experiment probes directly the time correlations of orientational order, and the QLRO regime is bounded by long correlation times. When the liquid crystal is more than a few degrees below the SmC-SmA phase transition temperature (away from $k_BT=\pi K$) we should see this logarithmic decay with ease. Figure 7 shows data for the two cases probing predominantly splay fluctuations and predominantly bend fluctuations spanning a range of time scales.

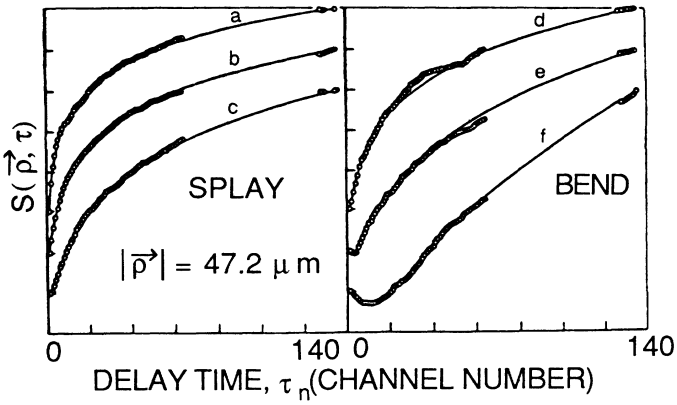

FIG. 7. Plots of $S(\boldsymbol{\rho},\tau_n)=\Xi(\boldsymbol{\rho},\tau_1,\tau_n)/\Xi(\boldsymbol{\rho},\tau_1,\tau_N)$ with $N=136$ are shown. The data (a), (b), and (c) are the splay case $\chi=\pi/2$ at 74.8 °C fit with $D_S=1.3\times10^{-4}$ cm^2/sec. The time delays between first and last data points τ_N are (a) 50 sec, (b) 6 sec, and (c) 1.5 sec. A fit of (a) to $\ln(n)/\ln(N)$ is indistinguishable from the fit using Eq. (31) shown. The data (d), (e), and (f) are the bend case $\chi=0$ at 66.5 °C and are fit with $D_B=1.1\times10^{-5}$ cm^2/sec. The values of τ_N are (d) 40 sec, (e) 10 sec, and (f) 2.5 sec. Including the $\delta\Phi(\delta\Phi)^3$ terms has enabled good fits to the anticorrelation observed especially in (e) and (f).

Figures 7(a)–7(c) show $S(\boldsymbol{\rho},\tau_n)$ for the splay case ($\chi=\pi/2$) for a fixed probe separation ($\rho=47.2$ μm) and for three delay time ranges, respectively, $\tau_N=1140\tau_c$, $\tau_N=140\tau_c$, and $\tau_N=35\tau_c$, where $\tau_c=\rho^2/4D_S=4.3\times10^{-2}$ sec is obtained as a fitting parameter. Here, since we are considering particularly the long-time behavior of $S(\boldsymbol{\rho},\tau_n)$, we ignore corrections due to finite probe size and the $\delta\Phi(\delta\Phi)^3$ terms. The $\delta\Phi\,\delta\Phi$ terms yielded exponential integrals with arguments of the form $u=\tau_c/\tau_n$. For small u, $E_1(u)=-\gamma-\ln(u)+u-O(u^2)$. For $u<0.1$, to very good approximation,

$$S(\boldsymbol{\rho},\tau_n)\approx\frac{-\ln\left[\frac{\rho^2}{4D\tau_1}\right]+\ln\left[\frac{\rho^2}{4D\tau_n}\right]}{-\ln\left[\frac{\rho^2}{4D\tau_1}\right]+\ln\left[\frac{\rho^2}{4D\tau_N}\right]}=\frac{\ln(n)}{\ln(N)}\ , \qquad (48)$$

where n ranges from 1 to N. Since N is the same for all data the normalized correlation function $S(\boldsymbol{\rho},\tau_n)$ approaches an asymptotic logarithmic form which is scale invariant (independent of τ_1). This scale-invariant divergence is distinctive of the Landau-Peierls instability. For the longest time scale splay data shown in Fig. 7(a), $u_1=\tau_c/\tau_1\approx0.12$ and fitting $\ln(n)/\ln(N)$ to the data is indistinguishable from fitting with Eqs. (31) or (47). The data shown in Fig. 7(a) are the result of accumulating the correlation function for 4 h. The slowest time scales probed are fluctuations of 50-sec duration. In the illustration of splay data on shorter time scales shown in Figs. 7(b) and 7(c), the time scales are too short to observe solely logarithmic decay. To extract D_S in this experiment data must be obtained on short enough time scale to observe the exponential integral's polynomial departure from logarithmic decay.

For the bend case, rms fluctuations in Φ are larger than for the splay case and these large-amplitude fluctuations affect the data in a number of ways. Figures 7(d)–7(f) show $S(\rho,\tau_n)$ for the bend case ($\chi=0$) for $\rho=47.2$ μm and $\tau_N=78\tau_c$, $19\tau_c$, and $4.8\tau_c$, respectively, with $\tau_c=\rho^2/4D_B=5.1\times10^{-1}$ sec. As in Fig. 5(b), the data in Fig. 7(f) exhibit the initial decrease in $S(\rho,\tau_n)$ described as anticorrelation and understood as the contribution of the $\delta\Phi(\delta\Phi)^3$ terms to the intensity fluctuations. The fit to the data shown is one demonstration of the success of this idea. The anticorrelation may be understood realizing that orientation fluctuations of all wavelengths between the probe size and the sample size contribute to the cross-correlation function obtained. This continuum of lengths probed means both large-amplitude slow fluctuations and small-amplitude faster fluctuations are important. The slow fluctuations establish on average an initial anticorrelation of the intensity at the two detectors while the faster fluctuations are positively correlated eventually overwhelming the initial anticorrelation. As the time scale is increased [Figs. 7(e) and 7(d)] the relative effect of the $\delta\Phi(\delta\Phi)^3$ contribution decreases. There is no plot for the bend case of the scale-invariant logarithmic limit as was shown in Fig. 7(a) for the splay case. In the bend case to obtain $\tau_N=1140\tau_c$ as was obtained for the splay case the delay time per channel would need to be 4 sec and $\tau_N=580$ sec. To obtain comparable statistical accuracy as was obtained in 4 h for the data shown in Fig. 7(a), the correlator would have to accumulate for two days and have a modified sample time clock (the limit on the Langley Ford is $\tau_1=0.99$ sec). The data shown in Fig. 7(d) were obtained for $\tau_1=0.28$ sec and were accumulated for 12 h. Even in this case a long-wavelength fluctuation caused a deviation from theoretical fit.

Though we have concentrated on the value of $\tau_c=\rho^2/4D$ in this discussion of time dependence of the cross correlation function, τ_c is not the only parameter characterizing $S(\rho,\tau_n)$. That is, even for the same value of τ_c data obtained probing predominantly splay fluctuations will not superimpose with data probing predominantly bend fluctuations. This distinction is preserved formally in the integral Q_n as defined in Eq. (47). For the splay case $D/D'\approx7$, while for the bend case $D/D'\approx\frac{1}{7}$. This difference manifests itself for the $\delta\Phi\,\delta\Phi$ terms as shown in Fig. 6, reflecting the $\approx7°$ amplitude of splay fluctuations compared with the $\approx20°$ amplitude of bend fluctuations. The logarithmic decay in order characteristic of a 2D Landau-Peierls system has been explicitly observed in the splay case, and is implicitly observed in the fits for all data, even with $u>0.1$. The temporal behavior of the data has been presented by comparing different time scales for a single choice of $|\rho|$. Next we will examine the effect of changing the magnitude of ρ.

B. Spatial variation

Changing the separation of the probes in the image enables study of the decay in order as a function of distance. Orientational order in this 2D system should decay logarithmically and thermally driven fluctuations of all length scales from the effective probe diameter to the size of the sample should exist. The logarithmic spatial dependence and diffusive orientational dynamics lead to the theoretical scaling of the characteristic time as $\tau_c\propto\rho^2$. This scaling is modified when $|\rho|$ is comparable to the fiber-optic-probe diameter, though this effect is included in Eq. (47). We expect, for a single temperature, that data for arbitrary $|\rho|$ may be fit using Eq. (47), without variation of D or K. Figures 8 and 9 show data for a sequence of probe separations for the splay and bend cases, respectively. For both cases the effect of finite probe size at small $|\rho|$ is observed as a deviation from the uniform scaling $\tau\propto\rho^2$ seen at larger separations. All the data shown in Figs. 8 and 9 were obtained at 76.2 °C. The probe separation ranges from 14 to 150 μm. This range in separation means we are studying correlated fluctuations of about 10^9 to 10^{12} molecules for the five-layer film used.

Obtaining data on index of refraction fluctuations at these very large spatial separations involves novel experimental difficulties. The laser was used primarily to provide high-intensity illumination. Interference patterns are ubiquitous due to the use of monochromatic light, therefore the number of glass interfaces in the beam path should be minimized. The illumination area was limited by the optics used to an $\approx$50-μm-diam spot with a Gaussian beam profile, limiting the probe separation to ≈250 μm to obtain signals of similar average intensity at the two probes. Obtaining data at large separations

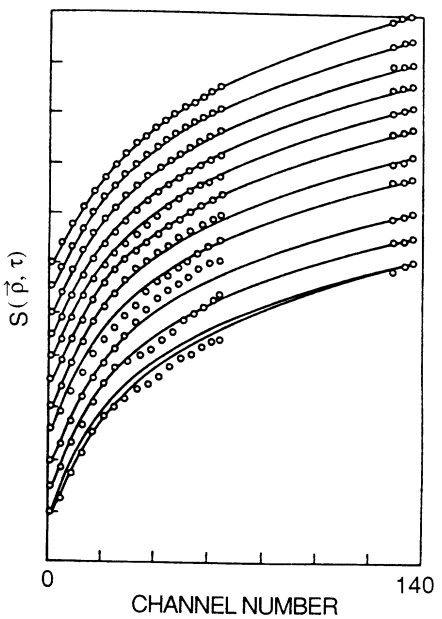

FIG. 8. Plots of $S(\rho,\tau_n)$ for the splay case ($\chi=\pi/2$) at 76.2 °C. From top to bottom the fibers center to center separation $|\rho|$ is 13.7, 17.1, 20.8, 24.0, 27.8, 31.3, 48.6, 66.1, 83, 118, and 153 μm. The time scale is determined by the delay per channel. The delay for channel No. 1 τ_1 increases as $|\rho|^2$ from 0.9 msec to 0.11 sec from top to bottom. All runs show the fit for $D_S=1.4\times10^{-4}$ cm^2/sec. The bottom run $|\rho|=153$ μm also shows the fit for $D_S=1.5\times10^{-4}$ cm^2/sec which does not fit the data nearly so well as $D_S=1.4\times10^{-4}$ cm^2/sec.

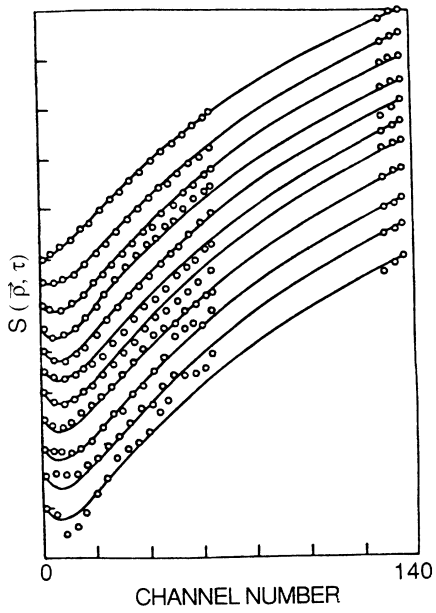

FIG. 9. Plots of $S(\rho,\tau_n)$ for the bend case ($\chi=0$) at 76.2 °C. $|\rho|$ and τ_1 vary exactly as for Fig. 6 from top to bottom. The fits are all using Eq. (49) with $D_B=2.3\times10^{-5}$ cm^2/sec. Note, in the bend case $\tau_c=\rho^2/4D$ is about six times τ_c in the splay case; data for equivalent $|\rho|$ and τ_1 must be accumulated for six times longer in the bend case than the splay case to obtain the same signal-to-noise ratio. The data for $|\rho|=153$ μm shown here were accumulated for 12 h and have a poor signal-to-noise ratio. Also, the last channel in the $|\rho|=153$ μm data is $\tau_1\times137=15$ sec delayed from the first channel.

necessitates long data acquisition times due to the $\tau\propto\rho^2$ scaling. For $\rho=50$ μm, a good signal-to-noise ratio is attained for each data set in about an hour. Increasing ρ to 500 μm would necessitate collecting data for approximately four days to obtain similar statistical resolution.

The data are fit with Eq. (47) to obtain the diffusion and elastic constants. As shown in Eq. (48), when τ_1 is chosen large enough all sensitivity to the physical parameters of the system is lost, since $\ln(n)/\ln(N)$ fits the data. When not in the limit of $S(\rho,\tau_n)\propto\ln(n)$, that is, for $\tau/\tau_c<10$, the shape of the curve defined by the data is sensitive to the value of D chosen for the fit to better than 10%. In particular, in fitting the nonmonotonic behavior, the choice of D affects primarily the value of $\tau_{\min}$, the time for which $\partial S(\rho,\tau_n)/\partial\tau=0$. Decreasing D causes $\tau_{\min}$ to increase. The choice of $A_4=4k_BT/\pi\sqrt{K_SK_B}$ affects primarily the depth of the minimum, therefore minimizing τ_1 maximizes the sensitivity to the actual value of $\sqrt{K_SK_B}$. Since orientation fluctuations of long enough wavelength to change the average orientation probed do exist χ may change during a run. This is particularly disturbing in the bend case since even if $\chi=0$ is chosen at the beginning of a run, χ may be nonzero during some parts of the run, allowing a mixing of splay contributions to the bend data. This may increase the apparent best-fit diffusion constant. Usually when splay mixing occurs it is obvious as a discontinuous decay in the data. We believe the noise in the large $|\rho|$ data is due to slow changes in Φ_0. A mixing of bend into splay when $\chi=\pi/2$ has negligible effect on the resulting best-fit diffusion constant because $D_S\approx7D_B$. In spite of these difficulties reasonable values for the diffusion constants are found and the temperature dependences of D_S and D_B are obtained.

C. Diffusion constants

One characteristic which makes liquid crystals interesting systems to study is the richness of the phase diagrams associated with them. In the five-layer racemic DOBAMBC FSLCF the smectic-A phase is above 115 °C, the smectic-C phase between 66 and 115 °C, and the smectic-I phase below 66 °C. The SmC-SmA phase transition is quite interesting to study, being weakly first order. There is a continuous decrease in the tilt angle θ_T as the transition is approached from below. Unfortunately, this decrease is accompanied by a continuous reduction in the contrast observed in the depolarized image, making meaningful study using depolarized microscopy impossible for $T-T_{CA}<2$ K. On the other hand, we easily and clearly observe the SmC-SmI phase transition. Observing the SmC phase by eye we see large-amplitude orientation fluctuations appearing as a random flickering of bright and dark regions. These regions are geometrically anisotropic and seem to have characteristic dimensions of 10×50 μm with the extended region perpendicular to $\hat{\mathbf{C}}(x,y)$. We interpret this as the size of the fluctuations which have a characteristic lifetime equal to the integration time of the human imaging system. As the temperature of the FSLCF is lowered through the SmC-SmI transition the characteristic dimension of the fluctuating regions decreases by about an order of magnitude. Continuing to decrease the temperature seems to produce little change in the fluctuations and at about 30 °C the film breaks on solidification. The cross correlation data show characteristic changes as a function of temperature which are not obvious from the form of Eq. (47). As temperature is increased, keeping fixed probe separation and sample time, the amplitude of the anticorrelation in the bend case decreases continuously and for $T>90$ °C the data become monotonic. As T is raised above 100 °C the signal becomes too small relative to the noise to fit the data. As T is lowered the amplitude of anticorrelation in the bend case increases steadily in the SmC phase. At 66 °C, the SmC-SmI transition, the amplitude of anticorrelation and $\tau_{\min}$ increase very rapidly and continue to increase as T is lowered in the SmI phase. Splay fluctuations exhibit less dramatic changes across the transition. There is essentially no qualitative change as a function of T in the SmC phase, while in the SmI phase the noise in the correlation data increases rapidly. An understanding of these effects is obtained through analysis of the diffusion constants obtained from best fit.

The existence of an anisotropy in the diffusion constants determined from the data has been the subject of considerable discussion to this point. It has been experimentally established that this anisotropy is a function of χ reflecting the relative orientation of $\hat{\mathbf{C}}$ and ρ. In partic-

ular, the smallest values of D are obtained when $\chi=0$. The largest values of D are obtained when $\chi=\pi/2$. The existence of two modes of relaxation for orientation fluctuations, splay and bend, has also been discussed. The conclusion drawn based on these observations is that there are characteristic diffusion constants for splay and bend of the director. These have been designated D_S and D_B, and their values are experimentally determined from fits to Eq. (47). If they are separable as was assumed in the anisotropic correction to the 2D XY model then $D_S=K_S/\eta$ and $D_B=K_B/\eta$. Estimates of D_S and D_B may be extrapolated from Rosenblatt's measurements of K_S and K_B, and η. This consistency with earlier experimental results, and agreement with theoretical predictions, suggests conclusions might be drawn based on the temperature dependence of the experimentally determined diffusion constants.

We have demonstrated in Figs. 7–9 that good fits to data in the SmC phase are possible and we believe that the values of the diffusion constants obtained by fitting Eq. (47) to the data are the actual splay and bend orientational diffusion constants. Attempting to use the same theory to fit data in the SmI phase becomes less and less satisfying with decreasing temperature. Smectic-I data near the SmC-SmI transition temperature are shown in Fig. 10. We observed visually that fluctuations of a particular wave vector are much slower in the SmI phase than in the SmC phase. These slow fluctuations have been quantified by CCIFS, but the signal-to-noise ratio becomes so small that the functional form is unresolved and the decay time becomes too slow to observe with the correlator. As the temperature decreases the decay in the splay case become almost linear. In the bend case obtaining reproducible values of $\tau_{\min}$ and the anticorrelation amplitude becomes impossible. A "best" fit to any particular data set is possible though, and values for D_S and D_B are extracted.

The best fit values of diffusion constants for splay and bend vs temperature are shown in Fig. 11. The data were

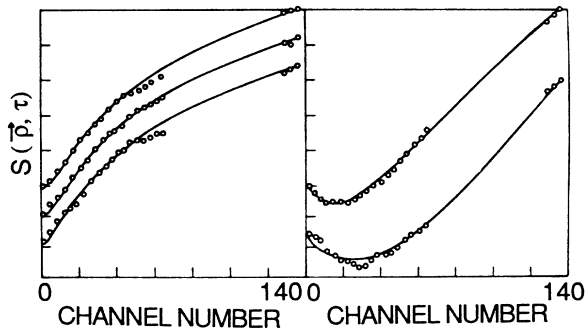

FIG. 10. Splay data (on the left) and bend data are shown for the smectic-I phase of DOBAMBC. For all runs, $\rho=47.2$ μm. From top run to bottom the splay data are obtained at $(T,\tau_1)=66.0$ °C, 44 ms; 64.4 °C, 70 ms; and 61.8 °C, 140 ms. The fits shown for these runs are with $D_S=1.1\times10^{-5}$, 7×10^{-6}, and 3.5×10^{-6} cm^2/sec, respectively. The bend data shown are for $(T,\tau_1)=64.4$ °C, 72 ms and 57.1 °C, 140 ms. The best-fit diffusion constants are $D_B=1.4\times10^{-6}$ and 4.5×10^{-7} cm^2/sec.

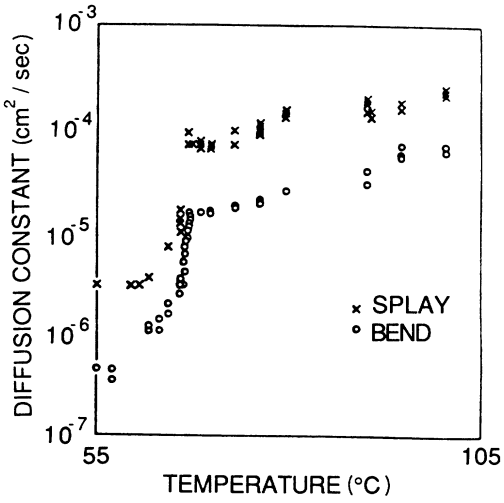

FIG. 11. The temperature dependence of $D=K/\eta$ is shown for the splay and bend cases. The abrupt decrease in both D_S and D_B at 66 °C is associated with the quenching of orientation fluctuations at the SmC-SmI phase transition. Each datum is the result of a best fit for a different experimental run. All data were obtained from the same five-layer film.

obtained over the course of two months from a single five-layer DOBAMBC film. Both diffusion constants decrease by a factor of 2 as temperature is lowered from 100 to 66 °C while remaining in the SmC phase. In the temperature interval he explored, Rosenblatt's data[7,25] predicts temperature-independent diffusion constants. He found that K_S, K_B, η_S, and η_B all increased linearly with decreasing temperature in the range 115 to 90 °C for a three-layer DOBAMBC film. Since $D=K/\eta$, we would expect that if K and η remain linear functions of T down to 66 °C the corresponding diffusion constants would be independent of T. There is an abrupt decrease, by an order of magnitude for both D_S and D_B, at 66 °C, the SmC-SmI transition temperature. The SmI phase is distinguished from the SmC by an increase in local orientational order. In both the SmC and the SmI translational order is short range. We would expect this enhanced orientational order in the SmI to be accompanied by an increase in both the elastic constants and viscosities. Our observation of a decrease in the diffusion constants indicates the orientational viscosity is increasing faster than the increase in orientational elastic constants. It would be quite interesting to study the behavior of the elastic constants and viscosities in more detail across the SmC-SmI transition.

V. CONCLUSIONS

Freely suspended liquid-crystal films are unique and fundamentally very interesting systems to study. They exhibit the highest free surface-to-volume ratio attainable in a stable system. This encourages study of surface properties and suggests the possibility of observing 2D effects. Also, as for all liquid-crystalline systems, the study of phase transition behavior in the films is interest-

ing. We have studied the fluctuation dynamics of the orientation field defined by $\hat{C}(x,y)$ in a thin tilted smectic FSLCF. Orientational order is observed to decay logarithmically as expected in the quasi-long-range-order regime of a real 2D system. In addition, we have observed the change in order across the Sm*C*-Sm*I* phase transition in the film.

This study was made using cross-correlation intensity-fluctuation spectroscopy to study the decay in order in real space and time. It is easy to observe fluctuations of very long length scale in the depolarized real image of the tilted smectic film. The nature of these thermally-driven long-wavelength fluctuations was quantified by cross correlating in real time the intensities at spatially separated probes in the depolarized image of the film. The data obtained verified the two dimensionality of the system by exhibiting directly the logarithmic decay in order at long times and over large distances. The spatial scale of fluctuations studied by this method is longer than can be studied in light-scattering experiments.

In studying these very long-wavelength fluctuations, effects not normally important in scattering experiments affect the data. The elastic constants associated with splay, bend, and twist of $\hat{n}(r)$ in a 3D nematic are of about the same magnitude, and fluctuations about $\langle \hat{n}(r) \rangle$ are of small amplitude and limited extent. In the FSLCF twist is eliminated, at least for lengths longer than the film thickness, and the bend elastic constant is almost an order of magnitude smaller than the splay constant. The amplitude of long-wavelength thermally-driven bend fluctuations is so large that the intensity of depolarized light reflected from the film cannot be assumed to fluctuate only linearly with orientation fluctuations. This is distinct from the typical light-scattering experiment in which the scattered intensity is assumed to fluctuate linearly with the fluctuations in the index of refraction of the probed system. The nonlinear contribution leads to many complications in the analysis. In order to account for the anisotropy in elastic constants and the nonlinear contribution to the cross-correlation data some detailed analysis was required. We showed how this nonlinear contribution to the fluctuating intensity arises in the case of large enough amplitude orientation fluctuations. We also included the anisotropy in elastic energies to calculate the dynamics observed, so as to understand the values of the diffusion constants extracted from fitting the data. The consistency with which we were able to obtain splay and bend diffusion constants allowed a temperature profile of D_S and D_B in the Sm*C*, and to a limited extent in the Sm*I*, phase to be obtained. We found that the splay and bend orientational diffusion constants decrease with decreasing temperature in the Sm*C* phase. As the Sm*C*-Sm*I* transition is crossed from above both D_S and D_B decrease by an order of magnitude accompanying the optically observed quenching of fluctuations.

ACKNOWLEDGMENTS

The experiment was performed entirely at the University of Colorado as the major portion of the Ph.D thesis of one of us (D.H.V.W.), and was supported by National Science Foundation (NSF) Grant No. DMR-83--07157.

[1]G. Friedel, Ann. Phys. (Paris) **18**, 273 (1922).

[2]N. A. Clark and R. B. Meyer, Proceedings of the Vth International Liquid Crystal Conference, Stockholm, Sweden, 1974 (unpublished); C. Y. Young, R. Pindak, N. A. Clark, and R. B. Meyer, Phys. Rev. Lett. **40**, 773 (1978).

[3]J. Collett, P. S. Pershan, E. B. Sirota, and L. B. Sorensen, Phys. Rev. Lett. **52**, 356 (1984).

[4]B. I. Halperin and D. R. Nelson, Phys. Rev. Lett. **41**, 121 (1978); Phys. Rev. B **19**, 2547 (1979).

[5]D. E. Moncton, R. Pindak, S. C. Davey, and G. S. Brown, Phys. Rev. Lett. **49**, 1865 (1982).

[6]S. B. Dierker, R. Pindak, and R. B. Meyer, Phys. Rev. Lett. **56**, 1819 (1986); J. D. Brock, A. Aharony, R. J. Birgenau, K. W. Evans-Lutterodt, J. D. Litster, P. M. Horn, G. B. Stephenson, and A. R. Tajbakhsh, *ibid.* **57**, 98 (1986).

[7]C. Rosenblatt, R. Pindak, N. A. Clark, and R. B. Meyer, Phys. Rev. Lett. **42**, 1220 (1979); C. Rosenblatt, R. B. Meyer, R. Pindak, and N. A. Clark, Phys. Rev. A **21**, 140 (1980).

[8]D. H. Van Winkle and N. A. Clark, Phys. Rev. Lett. **53**, 1157 (1984).

[9]DOBAMBC (decyloxybenzylidene-*p'*-amino-*w*-methylbutyl-cinnamate) is 2-(propenoic acid)-3-[4-[[[4-(decyloxy)phenyl] methylene]amino]phenyl]-2-methylbutyl ester.

[10]R. B. Meyer, L. Liebert, L. Strzelecki, and P. Keller, J. Phys. (Paris) Lett. **36**, L-69 (1975).

[11]J. M. Kosterlitz and D. J. Thouless, J. Phys. C **6**, 1181 (1973); J. M. Kosterlitz, *ibid.* **7**, 1046 (1974).

[12]D. J. Bishop and J. D. Reppy, Phys. Rev. Lett. **40**, 1727 (1978).

[13]M. R. Beasley, J. E. Mooij, and T. P. Orlando, Phys. Rev. Lett. **42**, 1165 (1979).

[14]A. P. Young, Phys. Rev. B **19**, 1855 (1979); J. Frolich and T. Spencer, Phys. Rev. Lett. **46**, 1006 (1981).

[15]L. D. Landau, E. M. Lifshitz, and L. P. Pitaevskii, *Statistical Physics*, 3rd ed. (Pergamon, New York, 1980), Part 1, p. 433; R. E. Peierls, Helv. Phys. Acta. Suppl. **11**, 81 (1974).

[16]P. G. de Gennes, Symp. Farad. Soc. **5**, 16 (1971); *The Physics of Liquid Crystals* (Oxford, London, 1974), p. 111.

[17]J. L. Eriksen, Phys. Fluids **9**, 1205 (1966); F. M. Leslie, Arch. Ration. Mech. Anal. **28**, 265 (1968); O. Parodi, J. Phys. (Paris) **31**, 581 (1970).

[18]P. M. Morse and H. Feshback, *Methods of Theoretical Physics* (McGraw-Hill, New York, 1953), p. 173.

[19]*Handbook of Mathematical Functions,* edited by M. Abramowitz and I. A. Stegun (Dover, New York, 1972), p. 228.

[20]W. G. Griffin and P. N. Pusey, Phys. Rev. Lett. **43**, 1100 (1979).

[21]Z. Kam and R. Rigler, Biophys. J. **39**, 7 (1982).

[22]N. A. Clark, B. J. Ackerson, and A. J. Hurd, Phys. Rev. Lett. **50**, 1459 (1983).

[23]M. A. Handschy, J. Phys. E **11**, 692 (1980).

[24]J. Ruth, N. A. Clark, and B. J. Ackerson, Bull. Am. Phys. Soc. **28**, 405 (1983).

[25]C. Rosenblatt, thesis, Harvard University, 1978 (unpublished).

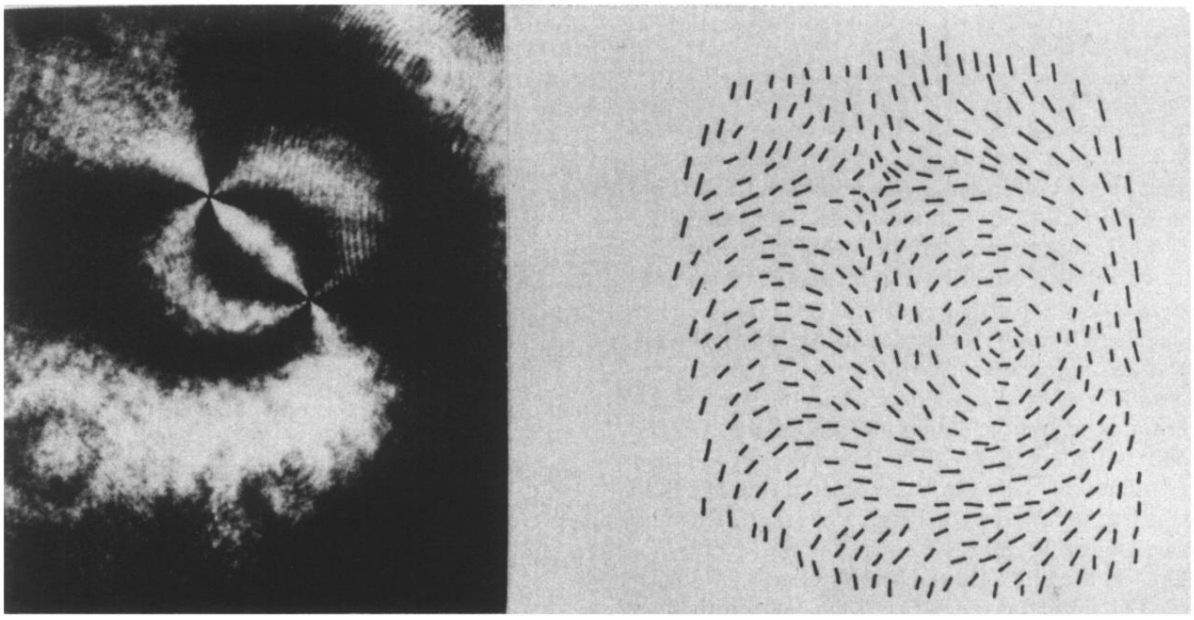

FIG. 3. A ± 1 disclination pair is illustrated. A photograph of the depolarized reflected image of a FSLCF of racemic DOBAMBC in its SmC phase illuminated with 488.0 nm light from an Ar-ion laser is shown. The film is "young" and disclination pairs formed in the spreading are still relaxing away, with this a photo of one those pairs. The film will thin to a uniform thickness and disclination pairs will annihilate, leaving a single $s = +1$ defect, within about an hour. The molecular orientation illustrating the disturbance of local order by the disclinations and the undisturbed region at the boundary is also shown.